Remote Sensing of Environment 334 (2026) 115203

Contents lists available at ScienceDirect

Remote Sensing of Environment

journal homepage: www.elsevier.com/locate/rse

Emulation-based self-supervised SIF retrieval in the O_2-A absorption band with HyPlant

Jim Buffat [a,d,*], Miguel Pato [b], Kevin Alonso [c], Stefan Auer [b], Emiliano Carmona [b], Stefan Maier [b], Rupert Müller [b], Patrick Rademske [d], Uwe Rascher [d], Hanno Scharr [a]

[a] Forschungszentrum Jülich GmbH, Institute of Advanced Simulation, IAS-8: Data Analytics and Machine Learning, Jülich, Germany
[b] Remote Sensing Technology Institute, German Aerospace Center (DLR), Oberpfaffenhofen, Germany
[c] European Space Agency (ESA), European Space Research Institute (ESRIN), Largo Galileo Galilei, Frascati, 00044, Italy
[d] Forschungszentrum Jülich GmbH, Institute of Bio- and Geosciences, IBG-2: Plant Sciences, Jülich, Germany

HIGHLIGHTS

- An emulator and a neural network are coupled for SIF retrieval.
- Validation with in-situ estimates indicates reliable accuracy and generalization.
- The approach allows pixelwise scene parameterization to model the radiative transfer.

ARTICLE INFO

Communicated by Dr Jing M. Chen

Keywords:
Sun-induced fluorescence
Deep learning
Hyperspectral sensors
Radiative transfer modelling
Spectral fitting methods

ABSTRACT

The retrieval of sun-induced fluorescence (SIF) from hyperspectral imagery requires accurate atmospheric compensation to correctly disentangle its small contribution to the at-sensor radiance from other confounding factors. In spectral fitting SIF retrieval approaches this compensation is estimated in a joint optimization of free variables when fitting the measured at-sensor signal. Due to the computational complexity of Radiative Transfer Models (RTMs) that satisfy the level of precision required for accurate SIF retrieval, fully joint estimations are practically unachievable with exact physical simulation. We present in this contribution an emulator-based spectral fitting method neural network (EmSFMNN) approach integrating RTM emulation and self-supervised training for computationally efficient and accurate SIF retrieval in the O_2-A absorption band of HyPlant imagery. In a validation study with in-situ top-of-canopy SIF measurements we find improved performance over traditional retrieval methods. Furthermore, we show that the model predicts plausible SIF emission in topographically variable terrain without scene-specific adaptations. Since EmSFMNN can be adapted to hyperspectral imaging sensors in a straightforward fashion, it may prove to be an interesting SIF retrieval method for other sensors on airborne and spaceborne platforms.

1. Introduction

Any application based on hyperspectral imagery of the earth's surface acquired from remote platforms must consider the influence of the atmosphere at acquisition time. The atmospheric state has a confounding influence on the measured at-sensor radiance. In order to disentangle atmospheric effects from any physical surface variable a firm understanding of the physical signal generation is necessary. Various atmospheric radiative transfer models (RTMs) have been developed (e.g. MODTRAN6 Berk et al., 2014, 6S/6SV Kotchenova et al., 2006, 2007, libRadTran Emde et al., 2016) to derive appropriate correction algorithms for these effects. In vegetation-related remote sensing it is crucial to couple such atmospheric models with leaf and soil optical properties, leaf-level energy fluxes (Jacquemoud et al., 1990; Feret et al., 2008; Tol et al., 2009a,b), and radiative transfer models in the canopy (Jacquemoud et al., 2009; Gastellu-Etchegorry et al., 2015) to enable accurate retrieval of biophysical parameters from remote sensing reflectances.

Similarly, the retrieval of sun-induced fluorescence (SIF) from hyperspectral imagery in atmospheric absorption bands relies heavily on

* Corresponding author at: Forschungszentrum Jülich GmbH, Institute of Advanced Simulation, IAS-8: Data Analytics and Machine Learning, Jülich, Germany.
Email address: j.buffat@fz-juelich.de (J. Buffat).

https://doi.org/10.1016/j.rse.2025.115203
Received 24 February 2025; Received in revised form 22 November 2025; Accepted 12 December 2025
Available online 25 December 2025

accurate modelling of atmospheric radiative transfer and of sensor properties. The state of the atmosphere parameterized by its water vapour content, the type and density of aerosols at recording time as well as the pressure and temperature profiles along the optical path modulates the radiance signal from which SIF is retrieved (Pato et al., 2025; Daumard et al., 2015; Cogliati et al., 2015; Sabater et al., 2018). Since in typical airborne acquisition scenarios for SIF retrieval no atmospheric measurements are recorded, atmospheric variables are usually estimated using RTMs in iterative processes. However, RTMs often cannot be used directly in radiance-based estimation due to their computational cost. To reduce the retrieval dependency and the number of RTM simulations required to retrieve SIF from at-sensor radiance, a two-step procedure is assumed in various SIF retrieval methods as opposed to a joint estimation of surface, atmospheric and sensor related parameters.

In a first step, the atmosphere is characterized for a set of pixels to derive the atmospheric transmittance with the help of an RTM. In a second step, these transmittance estimates are used to disentangle reflectance, fluorescence and possibly sensor miscalibrations commonly parameterized in center wavelength (CW) and full width at half maximum (FWHM) shifts. For example, (Cogliati et al., 2019; Wieneke et al., 2016) derive a set of atmospheric transfer functions for single acquisitions using an RTM 'interrogation' technique first introduced by Verhoef and Bach (2003). Operationally, these estimated transfer functions are finetuned to account for retrieval errors of atmospheric components due to sensor noise, sensor miscalibration and model inaccuracies by modifications of a procedure called *transmittance correction* (Guanter et al., 2010; Damm et al., 2014). This type of finetuning of the atmospheric transfer functions is based on the presence of non-vegetated pixels that are not affected by fluorescence. The identification of non-vegetated soil pixels can be difficult, however, in many geographical areas and especially in observation setups resulting in pixel sizes larger than a few meters where *pure* pixels are rare.

The validity of constant atmospheric transfer across a large set of spatial pixels relies on auto-correlation distances of atmospheric factors in airborne imagery being usually larger than the spatial extent of the prediction (Anderson et al., 2003; Thompson et al., 2021). This usually results in the use of a single RTM estimate per acquisition. In the case of spaceborne acquisitions with much larger spatial footprints, as will be provided for example by the FLEX mission (Drusch et al., 2017), this assumption is not satisfied and strategies to localize the atmospheric characterizations efficiently must be developed. In the context of atmospheric correction for accurate reflectance estimation (Thompson et al., 2022) have for example recently demonstrated the use of local linear emulators for accurate and computationally efficient atmospheric correction.

Similarly to changing atmospheric conditions on spatial scales relevant to satellite observations, the strongly changing observational conditions in airborne observations of topographically variable terrain are a challenge for SIF retrieval algorithms based on spectral regions affected by O_2 absorption. The simplifying assumption of constant atmospheric transmittance is invalid in these cases since the resulting optical path differences cause large variance in the depth of these absorption features.

Buffat et al. (2025a) have proposed a pathway to computationally efficient SIF retrieval in these conditions by introducing the Spectral Fitting Method Neural Network (SFMNN). A reconstruction based on a Principal Component Analysis (PCA) of atmospheric transfer functions is used to model the radiative transfer nonparametrically in this approach. This allows for localized radiative transfer estimations and, importantly, a joint retrieval of the transfer functions as well as surface and sensor related quantities. However, the PCA loadings are fitted non-parametrically since they are not formulated as functions of physical quantities (e.g., surface and sensor altitude, water vapour content, aerosol optical density) as would be the case with physically explicit RTM simulations. This (i) impedes the explanatory power of atmospheric estimates and (ii) does not allow for constraining the atmospheric estimates with known physical quantities.

In this work, we propose the use of RTM emulation instead of the PCA-based radiative transfer formulation adopted in SFMNN to increase its physical accuracy in HyPlant FLUO data. Such an emulator-based SFMNN (EmSFMNN) approach has recently been validated for spaceborne DESIS data (Buffat et al., 2025b) in conjunction with a loss formulation similar to the original SFMNN approach (Buffat et al., 2025a). The authors find good agreement between their DESIS derived SIF estimates and HyPlant-based SIF estimates in a benchmark dataset consisting of quasi-simultaneously recorded HyPlant and DESIS acquisitions. The results of this study highlight the potential of the SFMNN approach for hyperspectral sensors with improved spectral sampling such as HyPlant FLUO and the FLORIS sensor onboard the ESA's Earth Explorer Mission FLEX (Drusch et al., 2017).

RTM emulation can be regarded as a computationally efficient approximation of the exact simulation by a function acting on the same input parameter space as its RTM counterpart (Servera et al., 2022). The functional form of such emulators is not relevant a priori, but depends on the application specifications such as the required computational speed, the reconstruction performance, the spectral range and the input parameter dimensionality. In this contribution, we derive a polynomial emulator from a large simulation database replicating typical observational conditions and the sensor characterization of the hyperspectral imaging sensor system HyPlant based on prior analysis published in (Pato et al., 2025, 2024, 2023). In this contribution, we show that extending this emulator to represent bandwise spectral miscalibration is integral for accurate SIF retrieval in HyPlant data. The functional form of the proposed extension matches well with the specific requirements of neural network training. The computational efficiency of its predictions and gradient computation is sufficient for training on large hyperspectral databases. With this novel neural network approach to integrate a computationally efficient model of canopy level optical properties and atmospheric radiative transfer into a SIF retrieval scheme, we are able for the first time to make use of a pixelwise geometrical parametrization for a joint estimation of SIF and reflectance in airborne SIF retrieval.

In this study, we focus on SIF retrieval of selected campaign data sets of the hyperspectral HyPlant sensor system (Siegmann et al., 2019; Buffat et al., 2024a). The sensor characteristics of HyPlant and the size of HyPlant data sets are uniquely suited to develop and improve partly data-driven SIF retrieval algorithms such as ours. Since HyPlant data is often acquired during field campaigns featuring ground based SIF measurements, we are able to complement the present study with a direct comparison of SIF estimates of our approach with ground-based in-situ SIF estimates. However, we point out that while HyPlant is well suited to test the setup presented in this work, EmSFMNN may be applied to data acquired by other airborne or spaceborne sensors. Its specific formulation is in fact well suited to cope with large existing hyperspectral data sets and continuous data streams of hyperspectral imaging sensors.

2. Data

2.1. Data quality provided by the HyPlant FLUO sensor

The HyPlant FLUO sensor (Siegmann et al., 2019) is the airborne demonstrator for the spaceborne FLEX satellite mission (Drusch et al., 2017). As such, it has been designed specifically for SIF retrieval in the atmospheric O_2-A and O_2-B absorption bands with a spectral sampling interval of 0.11 nm and a full width at half maximum (FWHM) of 0.25 nm. A large collection of hyperspectral HyPlant data sets have been collected since 2014 (European Space Agency, 2017a,b, 2018, 2019; Siegmann et al., 2021, 2022; Rascher et al., 2022) and are partly openly available (Buffat et al., 2024a), (Buffat et al., 2024b). In particular, yearly data sets since 2018 can be considered comparable across different campaigns due to the standardization of the radiometric calibration and the geometric correction. Overall, the radiometric

Table 1
Data sets of compiled HyPlant acquisitions from different locations in the years 2018–2023. *Data Set* denotes a single compilation. With *Campaign* we denote the campaign identifier pointing to the used acquisitions according to the identified scheme outlined in the openly available HyData data set (Buffat et al., 2024a), with *FLOX* we denote the availability of simultaneous FLOX data, with Δh the maximum topographic variation over the compiled data set, with *GSD* the physical ground sampling distance of individual pixels and with $|D|$ the data set size in terms of number of 60 × 60 px image crops. We report the number of patches used for training in parenthesis.

Data Set	Campaign	FLOX	Δh [m]	GSD [m]	$\lvert D\rvert$ [$\times 10^3$]	Location
SEL-2018 (600 m)	SEL	✓	20	1 × 1	15 (5)	Selhausen, DE
WST-2019 (1500 m)	WST	✓	20	2.3 × 2.3	14 (5)	Braccagni, IT
CKA-2020 (600 m)	CKA	✓	20	1 × 1	10 (3)	Kl. Altendorf, DE
CKA-2020 (350 m)	CKA	✓	20	0.5 × 1	8 (2)	Kl. Altendorf, DE
CKA-2021 (350 m)	CKA	✓	20	0.5 × 1	4 (1)	Kl. Altendorf, DE
TOPO	SOP, HOE *600 m* *2021–2023*	–	300	1 × 1	11 (3)	Jülich, DE Hölstein, CH
PRE	PHY, HOE CKA, SEL WST, NRS SOP, TR32 *350–1800 m* *2018–2023*	–	300	0.5–2.3	235 (38)	

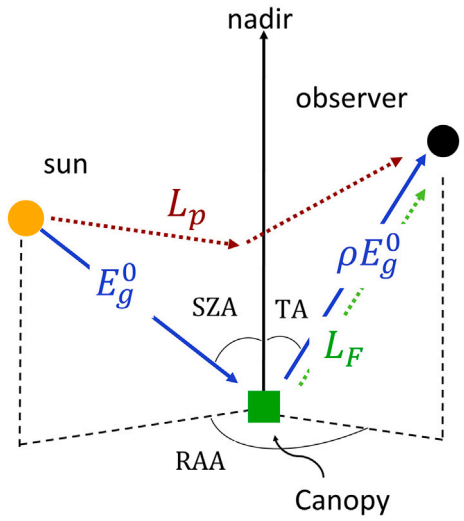

Fig. 1. Geometrical set-up of the sun-observer geometry definitions in use. *RAA* denotes the relative azimuth angle, *TA* the tilt angle and *SZA* the sun zenith angle.

calibration achieves a mean relative uncertainty r_g of 3 % (Rascher et al., 2022) and the geolocalization subpixel accuracy (Siegmann et al., 2019).

In this study, we make use of radiometrically corrected HyPlant FLUO acquisitions obtained during the years 2018 – 2023 (cf. Table 1) in different flight campaigns, various locations and varying sun–observer geometries. The dataset incorporates a large portion of all available HyPlant FLUO acquisitions from this time period. We notably include acquisitions with strong topographic variation to train and to test the retrieval performance under these demanding conditions (see Section 4.3).

2.2. Simulation of HyPlant at-sensor radiance

The emulator utilized in this work is based on the polynomial emulator described in (Pato et al., 2024, 2023) derived from a simulation tool generating single pixel at-sensor radiance (Pato et al., 2025). It uses MODTRAN6 to model radiative transfer through the atmosphere at 0.1 cm^{-1}. Simple parametric models are assumed for surface reflectance and fluorescence emission in the spectral range around the O_2-A oxygen absorption band. The parameters of the simulator have been chosen according to an extensive sensitivity study performed in (Pato et al., 2025). We fixed the ranges of the resulting 13 parameters (see Table 2) to cover the empirical distributions found in the HyPlant acquisitions used in this work. Appropriate ranges for the geometric parameters *sensor altitude above ground level* h_{agl}, *ground altitude* h_{gnd}, *relative azimuth angle* (RAA) and *tilt angle* TA could be established exactly from metadata provided with HyPlant data (cmp. Fig. 1). The ranges for the surface parameters and for the sensor characterization were also adopted directly from preparatory work in (Pato et al., 2024,

Table 2
Specification of the ranges of all physical variables necessary for the parameterization of the simulation tool. H_2O denotes vertical water vapour content, AOT_{550} the aerosol optical thickness at 550 nm, TA the sensor's viewing angle, SZA the solar zenith angle, RAA the relative azimuth angle, h_{gnd} the ground altitude above sea level, h_{agl} the sensor height above ground level. ρ_{740}, s and e denote bias, slope and curvature of the reflectance according to the reflectance model definition given in (Pato et al., 2025, 2024), F_{737} is the fluorescence amplitude at 737 nm (*: F_{737} is given in units of [mW/nm/sr/m²]). $\Delta\lambda$ and $\Delta\sigma$ denote wavelength and sensor resolution shifts.

Specification		Range
Atmosphere	H_2O [cm]	0.3–3.0
	AOT_{550} []	0.02–0.30
Geometry	TA [°]	0–25
	SZA [°]	20–55
	RAA [°]	0–180
	h_{gnd} [km]	0–0.760
	h_{agl} [km]	0.2–2.86
Surface	ρ_{740} []	0.05–0.60
	s [nm^{-1}]	0–0.012
	e []	0–1
	F_{737} [*]	0–8
Sensor	$\Delta\lambda$ [nm]	[−0.080, +0.080]
	$\Delta\sigma$ [nm]	[−0.040, +0.040]
Input dimensions		13
Number of bands		349
Number of samples		6.3×10^6

2023). The parametrization of a simple quadratic reflectance model implemented in the simulation tool was adopted according to an analysis of vegetation and soil reflectance spectra of the DUAL hemispherical-directional reflectance product that is computed operationally for all HyPlant acquisitions. Equally, we simulated fluorescence emission in the O_2-A band according to the top-of-canopy fluorescence emission model adopted by Pato et al. (2025) as a Gaussian with fixed mean (μ = 737 nm), fixed standard deviation (σ_f = 20 nm) and a free amplitude F_{737}. The ranges regarding the sensor characterization parameterized by center wavelength shifts $\Delta\lambda$ and FWHM shifts $\Delta\sigma$ were derived from in-flight data. Due to the lack of simultaneous measurements, which would have allowed estimates of aerosol optical thickness AOT_{550} and water vapour density H_2O, these ranges were chosen such that they covered all possible atmospheric states in which HyPlant campaigns are operated (cloud-free weather conditions in mid-latitude regions in summer).

We sampled the parameter ranges in Table 2 with different sampling strategies for the training and validation data set to derive an emulator as outlined in (Pato et al., 2024, 2023). Importantly, the input parameters p were sampled independently. Since the parametric models for the spectral shapes of the reflectance and fluorescence implemented in the simulation tool were completely independent as well, we prevented our retrieval method from incorporating cross-correlations between fitted parameters a priori. This would have undermined the purely physical approach followed in this work.

2.3. In-situ SIF validation data

For a subset of the HyPlant acquisitions used in this work in-situ measurements of SIF are available (see Table 1). All in-situ measurements were derived using the Improved Fraunhofer Line Discrimination Method (iFLD) (Alonso et al., 2008) from radiance point measurements and solar irradiance recordings of the hyperspectral FLOX device (Fluorescence Box, JB-Hyperspectral Devices GmbH, Duesseldorf, Germany). In the case of the FLOX measurement series matching with CKA-2020 HyPlant acquisitions, the in-situ measurements were taken at four different locations by four different devices. One FLOX was placed in an agricultural oat field and three others in wheat fields. For the validation, we have aggregated the time series and did not differentiate between the different FLOX devices. The localization of those FLOX systems was improved with an exact GPS RTK measurements at each of the devices. In the case of the in-situ measurements matching the SEL-2018 HyPlant acquisitions, a single mobile FLOX device was used in agricultural fields of sugar beet and wheat.

FLOX measurements falling within five min of the acquisition time of HyPlant were considered. We selected only FLOX measurements flagged as having high radiometric stability (< 1 % difference in solar irradiance over the course of the measurement) in order to exclude measurements affected by cloud and haze. Since HyPlant campaigns are only conducted in optimal weather conditions, no measurements had to be excluded. In the case of multiple measurements within this time window matching a single acquisition, we averaged the FLOX iFLD SIF estimate to compare with HyPlant derived SIF estimates. In order to account for localization errors as well as the field of view, we compared HyPlant pixels within a fixed 2 px radius around the measurement location, resulting in aggregation radii of 1 m, 2 m and 4.6 m for acquisitions acquired at 350, 600 and 1500 m above ground level (compare Table 1). The temporal and spatial variance resulting from the time windowing and spatial localization buffer were used as proxies for uncertainty estimates in the performance calculations.

3. Methods

In this work, we extend the Spectral Fitting Method Neural Network (SFMNN) setup first outlined by (Buffat et al., 2025a) with a simulation and emulation framework to improve the representation of the atmospheric radiative transfer (see flow chart in Fig. 2). SFMNN combines neural network training and physical radiative transfer simulation to estimate a decomposition of the at-sensor signal into constitutive quantities. In a first step, the spectral data is projected to a learnable spectral embedding space through a spectral encoder (see Fig. 3). From this common embedding space, a set of decoder heads estimates various physical variables. During inference these variable estimates are used directly as method products such as, e.g., the SIF product which is the estimated fluorescence. To train this estimation, the network passes these variables into a fixed simulation layer representing the physical radiative transfer to the sensor given the estimated variables. Training, thus, consists in aligning the spectral input with the simulated radiance spectra based on the network estimates. While in SFMNN (Buffat et al., 2025a) the simulation layer is defined as a simplified four stream model, we propose in this contribution the use of a polynomial emulator approximating the simulations of a radiative transfer simulation tool at high inference speeds (see Fig. 2). In the following paragraphs we first outline the network architecture and then describe the implementation and derivation of the emulator for the purpose of network training.

3.1. Neural network architecture

We construct a neural network acting on fixed size excerpts of HyPlant imagery (60 × 60 px) that we will refer to as *patches*. This patch size has not been tuned to optimize performance considerations in this

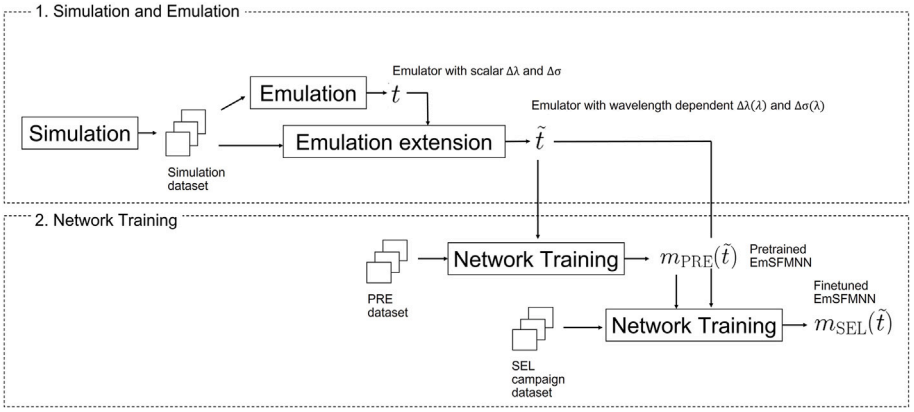

Fig. 2. Flowchart of the proposed EmSFMNN retrieval approach. In a first step, an emulator t is derived from a large simulation data set of HyPlant radiances in the O_2-A absorption band featuring variable surface conditions and observation geometries. The emulator t is extended to an emulator $\tilde{t}$ supporting wavelength dependent sensor shifts $\Delta\lambda(\lambda)$ and $\Delta\sigma(\lambda)$ according to the procedure detailed in Appendix A. In a second step, a SFMNN (Buffat et al., 2025a) is trained with $\tilde{t}$ as simulation layer. This training is conducted in two steps where a backbone network m_{PRE} is trained on a large data set of HyPlant acquisitions recorded in variable conditions. m_{PRE} is subsequently finetuned to individual, smaller data sets recorded under similar conditions (see Table 1), for example m_{SEL}.

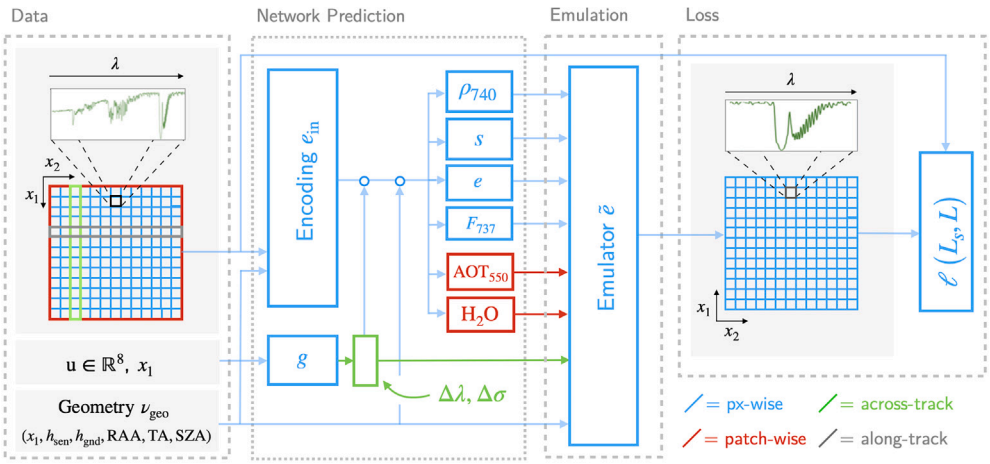

Fig. 3. Outline of the architecture and emulator integration of the SFMNN used in this work. Dimensions of the encoder e_{in}, the decoders for variables ρ_{740}, s, e, F_{737}, AOT_{550} and H_2O and the sensor characterization g are given in Table 3.

work, but set a priori. The network architecture is defined as a Multilayer Perceptron (MLP) encoder-decoder setup as in the original SFMNN formulation (Buffat et al., 2025a) and similarly to an earlier EmSFMNN implementation for DESIS (Buffat et al., 2025b) (see Table 3). The network is trained to predict all parameters $\vec{p}$ of the RTM model in Eq. (1) that cannot be inferred from metadata or geometrical recordings, i.e., all parameters in Table 2 except parameters of the group *Geometry*.

The encoder e_{in} and decoder modules d_v in this network are constructed as MLPs with residual links and have the dimensionalities given in Table 3. The decoders are tasked with disentangling the latent space spanned by the encoder to the physical parameters $\vec{p}$ parameterizing the radiative transfer model underlying the simulation tool and, thus, the emulator. We define two decoders d_v: one for the reflectance and fluorescence related parameters predicted for each pixel and one for the atmospheric parameters predicted for each patch. These two decoder modules are implemented identically with except for a final spatial mean reduction before the emulator layer in the case of the patchwise predictor. As in SFMNN, we differentiate between pixel-wise and patch-wise prediction based on the fact that atmospheric parameters (AOT and H_2O) have an autocorrelation that typically exceeds the physical patch size such that a single atmospheric estimate per patch can be assumed to lead to sufficiently precise approximations.

The estimation of sensor shifts $\vec{\Delta\lambda}$ and $\vec{\Delta\sigma}$ is implemented differently. We assume that we can fit these shifts as a function of the sensor state at acquisition time and the across-track sensor position alone without any spectral input. This assumption is implemented in the architecture by estimating the sensor shifts only from an arbitrarily defined acquisition identifier $\vec{u} \in \mathbb{R}^U$ that represents the sensor state and the across-track position x_1. At the start of the training we randomly instantiate these identifiers $\vec{u}$ of fixed dimensionality ($U = 8$) for each acquisition in the training dataset and include them as learnable parameters in the optimization. The MLP module g predicts shifts $\vec{\Delta\lambda}$ and $\vec{\Delta\sigma}$ for each wavelength ($\Lambda = 349$) at across-track positions x_1 from pixelwise concatenations of the identifier vectors $\vec{u}$ and a positional encoding of $\vec{x}_1$ (Vaswani et al., 2023).

An important characteristic of this particular setup consists in the physically coherent separation of inputs and the differentiation of output dimensions for individual parameters. For example, all reflectance parameters (ρ_{740}, s, e) and the fluorescence emission amplitude F_{737} are estimated for each pixel from the radiance data and geometrical information ν_{geo}, but without providing the acquisition identifier u since the decoders to those parameters by definition do not depend on sensor characteristics or acquisition dependent changes. Similarly, atmospheric parameters are estimated from radiance and ν_{geo} alone, but, differently from the surface parameters, only per patch as we assume negligible variance of these parameters over small spatial distances. The sensor characterization $\Delta\lambda$ and $\Delta\sigma$ on the other hand is uniquely estimated from the acquisition identifier u for individual across-track positions x_1 since it is driven by factors that are identical across single acquisitions. Both input separation and differentiation in output dimensionality constrain the network optimization architecturally with prior knowledge of the physical processes and sensor design at play. On the other hand, we implicitly constrain the network by enforcing physically accurate solutions of the radiative transfer equation Eq. (1) given a particular parametrization $\vec{p}$. Differently from the simplified four-stream model used in SFMNN to model at-sensor radiances, the emulator $\tilde{t}$ allows for pixel-wise parametrization of the radiative transfer formulation with known geometrical variables. This is a significant improvement over SFMNN's formulation as the solution space of the network can be constrained very precisely in a pixel-wise fashion.

Table 3
Dimensionalities for different modules in the EmSFMNN architecture (see Fig. 3). Elements in a tuple denote an architecture parameter for a single sublayer in a module. *Reps.* denotes the number of repetitions of linear layers in a sublayer, D_p denotes the dropout rate of the output of the sublayer. For a more detailed exposition of the module architecture we refer to (Buffat et al., 2025a).

Module	Parameters	
Encoder e_{in}	*Dim.*	(2e3, 2e3, 1e3, 5e2, 5e2, 1e2, 1e2, 1e2, 50)
	Reps.	(3, 3, 3, 3, 3, 3, 3, 1, 1)
	D_p	(0.05, 0.05, 0.01, 0.01, 0.005, 0.0)
Decoder d_v	*Dim.*	(1e2, 50, 50, 50, 10)
	Reps.	(3, 2, 2, 1)
	D_p	(0.05, 0.05, 0.01, 0.01, 0.005, 0.0)
Sensor charact. g	*Dim.*	(1e2, 50, 50, 50, 10)
	Reps.	(3, 2, 2, 1)
	D_p	(0.05, 0.05, 0.01, 0.01, 0.005, 0.0)

3.2. Simulation tool

A MODTRAN-based simulation tool is utilized in this work (Pato et al., 2025, 2024, 2023) to simulate the HyPlant at-sensor radiance in a spectral range covering the O_2-A absorption band (740–780 nm) according to the model

$$L_s(\vec{p}) = \left(L_p + \frac{E_g^0 \rho T^{\uparrow}}{\pi(1-\rho S)} + L_F T^{\uparrow} \right)(\vec{p}) \tag{1}$$

as a function of the parameters $\vec{p}$ (as defined in Table 2) where L_p is the path radiance, E_g^0 is the global solar irradiance on the ground, $T^\uparrow$ is the total transmission coefficient from surface to sensor (direct and diffuse components, $T^\uparrow = T^\uparrow_{\text{dir}} + T^\uparrow_{\text{dif}}$), L_F is the top-of-canopy fluorescence emission modelled as a Gaussian with fixed variance and amplitude F_{737}, S is the spherical albedo of the atmosphere, ρ is the hemispherical-directional reflectance modelled as a 2nd order polynomial with offset ρ_{740}, slope s and curvature e, H_2O denotes the columnar water vapour content, AOT_{550} the aerosol optical thickness, TA the viewing angle, SZA the solar zenith angle, RAA the relative azimuth angle between observation and irradiance directions, h_{gnd} the topographic height above sea level, h_{agl} the sensor height above ground level and $\Delta\lambda$ and $\Delta\sigma$ the scalar shifts in the center wavelength and full width at half maximum (FWHM). In order to be consistent with in-situ reference fluorescence estimates, we report SIF_{760} instead of F_{737} in all validation and analysis sections which we define as the functional value of the modelled fluorescence emission at 760 nm. The simulations have been conducted with an atmospheric model corresponding to the MODTRAN *mid-latitude summer* model. Thus, we have disregarded changes in the atmospheric pressure profile that might be caused by changing meteorology or topography. Concerning further simulation configuration details adopted in this work, we refer to prior work published by (Pato et al., 2025). Finally, as in (Pato et al., 2023, 2024), we densely sample the parameter space spanned by the parameter ranges in Table 2 and run a total of 6.3×10^6 simulations.

3.3. Emulator definition

Emulation of a hyperspectral simulator $L_s(\vec{p}) : \mathbb{R}^M \to \mathbb{R}^\Lambda$ from physical parameters $\vec{p} \in \mathbb{R}^M$ (see Table 2) by an emulator t is ultimately a regression problem where we derive a function $t : \mathbb{R}^M \to \mathbb{R}^\Lambda$ that reproduces as closely as possible the simulator L_s at reduced computational cost. In practice, there is a trade-off between reducing the residual between the simulator and emulator on the one hand and reducing the computational cost of t on the other for any non-trivial simulator L_s. Since the emulator is used during the training of a neural network, we require additionally that its gradient computation is efficient and preferably can be integrated easily into common programming frameworks for deep learning. The polynomial emulator investigated by (Pato et al., 2024, 2023) fulfills these requirements. It is defined as the polynomial function of d^{th} order

$$t_d(\vec{p} \mid \vec{a}_{\mathcal{K}^d}) = \sum_{\vec{k} \in \mathcal{K}^d} p_1^{k_0} \dots p_M^{k_M} \vec{a}_{\vec{k}}, \tag{2}$$

over the parameters $\vec{p}$, where $\vec{a}_{\vec{k}} \in \mathbb{R}^\Lambda$ and where the set of polynomial features is defined as

$$\mathcal{K}^d = \left\{ \vec{k} \in \mathbb{N}^M \; : \sum_{1 \le i \le M} k_i \le d \right\} \tag{3}$$

We train the emulator weights $\vec{a}_{\vec{k}}$ in a least-squares optimization on a training subset partitioned from the total simulation data set following (Pato et al., 2024, 2023). Throughout this work, we have chosen $d = 4$ since prior work (Pato et al., 2024) has shown this dimensionality to yield sufficiently accurate emulators for SIF retrieval in the O_2-A band. Accordingly, we drop the dimension demarcation and refer to t_4 as t in the rest of this contribution.

The emulator formulation in Eq. (2) is not adapted to cases where the physical parameters $\vec{p}$ are spectrally variable. This is particularly problematic when wavelength dependent shifts $\Delta\lambda(\lambda)$ and $\Delta\sigma(\lambda)$ need to be represented rather than scalar shifts. In the case of scalar shifts, as implemented in the original emulator definition of (Pato et al., 2024), the simulated spectra are exposed to the same simulated sensor miscalibration in all wavelengths. To improve the accuracy of the sensor model, we propose in this work the use of a computationally efficient reformulation of this emulator definition Eq. (2) allowing for wavelength dependent shifts $\Delta\lambda(\lambda)$ and $\Delta\sigma(\lambda)$. These reformulated emulators will be referred to as $\tilde{t}$. A detailed introduction and error analysis of this reformulation are provided in Appendices A and B.

3.4. Loss formulation

The loss used in this setup is adapted from the loss used in the SFMNN framework (Buffat et al., 2025a). It consists of a batchwise mean squared reconstruction error complemented by two regularizers. Given the input radiance spectra L_{HyP} as measured by HyPlant and matching geometrical metadata ν_{geo} (flight h_{sen} and ground altitude h_{gnd}, relative azimuth RAA, tilt angle TA and solar zenith angle SZA) we train the network n to minimize

$$\ell\left(L_{\text{HyP}}, \hat{L}_{\text{HyP}}\right) = \left\langle \left(L_{\text{HyP}} - \hat{L}_{\text{HyP}}\right)^2 \right\rangle_{\lambda, x} + \gamma_f \ell_f + \gamma_{\text{NDVI}} \ell_{\text{NDVI}}, \tag{4}$$

where L_{HyP} is the measured at-sensor radiance in the spectral window $\mathcal{W}$ and

$$\hat{L}_{\text{HyP}} = \tilde{t}(\tilde{\vec{p}}, \vec{\Delta\lambda}, \vec{\Delta\sigma}, \nu_{\text{geo}}) \tag{5}$$

denotes the network prediction with predicted $\tilde{\vec{p}}$, $\vec{\Delta\lambda}$ and $\vec{\Delta\sigma}$. $\langle \dots \rangle_{x,\lambda}$ denotes the spatial and spectral mean over the patches included in a batch. Throughout all experiments in this work we have fixed the regularizer weights $\gamma_f = 1$ and $\gamma_{\text{NDVI}} = 10$. These weights were established as they have shown satisfactory results in preliminary tests on the CKA-2020 (600 m) data set (see Table 1).

The fluorescence regularization

$$\ell_f = \left\langle \sum_{\lambda \in \mathcal{W}} w_\lambda \left(L_{\text{HyP}}(\lambda) - \hat{L}_{\text{HyP}}(\lambda)\right)^2 \right\rangle_x \Bigg|_{\delta p_i = 0,\, p_i \neq F_{737}} \tag{6}$$

boosts the contribution of reconstruction residuals according to an SNR-based weighting w_λ that accounts for the spectral distribution of typical fluorescence emission. This weighting is derived as the Moore-Penrose solution to a linearized retrieval problem with known reflectance and atmospheric parameters (Buffat et al., 2025a). We thus restrict the gradient contribution of this loss term to affect only the fluorescence decoder (i.e., network weights uniquely related to parameters $p_i \neq F_{737}$, reflectance, atmospheric and sensor parameters, are not affected by this term). The physiologically motivated regularizer

$$\ell_{\text{NDVI}} = \left\langle \hat{f} \cdot \delta\left(\text{NDVI} < \tau\right) \right\rangle_x \tag{7}$$

ensures that the fluorescence estimate f vanishes in pixels with very low green vegetation, i.e., in pixels with a low Normalized Difference Vegetation Index (NDVI). To identify these pixels, we set a threshold $\tau = 0.15$ on an approximate NDVI product derived from the radiance L_{HyP}.

3.5. Training setup

The training of the EmSFMNN SIF predictors takes place in two steps. We first train a backbone on the PRE HyPlant dataset (see Table 1). This backbone is used as the initialization to all EmSFMNN instances that are subsequently finetuned for individual datasets in a second step. Finetuning of PRE aims at adjusting the network (1) to the dataset-specific radiance calibration, (2) to train the acquisition specific identifiers u that determine the estimated shifts $\Delta\lambda$ and $\Delta\sigma$ and (3) to train in the specific parameter ranges covered differently in the various datasets (e.g. TOPO exhibiting larger variation of h_{agl}). During the finetuning step, the encoder e_{in} is fixed and only the decoders d_υ, the identifiers u and the sensor characterization g are trained. As the identifiers u are not estimated from the radiance data but rather implicitly as a result of the architectural constraint in each acquisition, there is no generalization property of this part of the network. Thus, in order to get meaningful shift predictions, a finetuning is thus necessary. When

EmSFMNN instances are applied to datasets for which they were not finetuned, arbitrary identifiers u are selected from the set of finetuned u. This procedure results in larger reconstruction errors than would have been possible with a finetuning of u but it doesn't necessarily affect the fluorescence estimate negatively. The spectral reconstruction window $\mathcal{W}$ was fixed to cover 750–770 nm.

4. Results

4.1. Reconstruction performance

We evaluate the impact of the various implemented constraints, the optimization and the emulator extension on the reconstruction performance. To this end, we compare the reconstruction performance of four different EmSFMNN setups to the reconstruction performance of an unconstrained least-squares optimization (LSQ) of the emulator t to individual pixels in a single HyPlant acquisition of the SEL data set (see Table 4). We show an extract of the studied HyPlant acquisition in Fig. 4. This comparison will allow (i) highlighting the effects of the training constraints and adoption of wavelength dependent shifts on the reconstruction performance, (ii) gauging gauge the generalization of reconstruction performance across similar HyPlant campaigns and (iii) assessing the impact of finetuning on the reconstruction performance. By $m_{\mathrm{CKA}}(\tilde{t})$ we denote an EmSFMNN predictor using the spectrally explicit sensor miscalibration emulator $\tilde{t}$ and finetuned on the CKA-2020 (600 m) data set. The EmSFMNN $m_{\mathrm{SEL}}(\tilde{t})$ and $m_{\mathrm{SEL}}(t)$ are equivalently trained on the SEL-2018 (600 m) data set and $m_{\mathrm{PRE}}(\tilde{t})$ denotes the common backbone without finetuning trained on the PRE data set. Importantly, the HyPlant acquisition for which we evaluate the reconstruction performance is part of the finetuning training set of $m_{\mathrm{SEL}}(\tilde{t})$ but not of $m_{\mathrm{CKA}}(\tilde{t})$. Due to the prediction of $\Delta\lambda$ and $\Delta\sigma$ in EmSFMNN being dependent on learnable IDs, and the ID not having been trained for $m_{\mathrm{CKA}}(\tilde{t})$, we use a single ID in CKA that we arbitrarily choose from the set of IDs trained for CKA acquisitions.

In Fig. 5 we report the distribution of the relative reconstruction residuals

$$\varepsilon = \left\langle \left| \frac{L_{\mathrm{HyP}} - \hat{L}_{\mathrm{HyP}}}{L_{\mathrm{HyP}}} \right| \right\rangle_{x,\lambda} . \tag{8}$$

of LSQ and all EmSFMNN predictors in the acquisition. We find that the unconstrained emulator optimization LSQ outperforms all EmSFMNN training setups in terms of reconstruction performance. However, since LSQ is completely unconstrained, the resulting estimates of physical parameters defining the simulation layer are not well disentangled. As a consequence, it cannot be used for SIF retrieval, even though it provides a useful baseline for the reconstruction error.

To first assess the impact of the feature-based setup and the training constraints of EmSFMNN, we compare $m_{\mathrm{SEL}}(\mathrm{t})$ to LSQ. Since the emulation layer of $m_{\mathrm{SEL}}(t)$ and LSQ are the same, a comparison of $m_{\mathrm{SEL}}(t)$ to the least-squares optimization LSQ isolates the impact of EmSFMNN's constraint formulation and its feature-based optimization. The direct EmSFMNN equivalent $m_{\mathrm{SEL}}(t)$ performs significantly worse than LSQ, presumably due to the constrained optimization. However, this decrease in reconstruction performance can be improved by adopting the extended emulator formulation with bandwise shift prediction which results in a smaller lower limit of the reconstruction residuals. Inclusion of wavelength dependent shifts also increases the tail towards larger residuals as can be observed from the error distribution of $m_{\mathrm{SEL}}(\tilde{t})$.

Secondly, to measure the generalization capacity of EmSFMNN across different data sets we compare $m_{\mathrm{CKA}}(\tilde{t})$ to $m_{\mathrm{SEL}}(\tilde{t})$. The residual distribution of $m_{\mathrm{CKA}}(\tilde{t})$ yields an ε which is significantly increased over its equivalent $m_{\mathrm{SEL}}(\tilde{t})$ as it lacks finetuning to the HyPlant input

Table 4
Definition of the EmSFMNN setups evaluated on the SEL-2018 acquisition of Section 4.1.

	Description
LSQ	Unconstrained least-squares fit of emulator $\tilde{t}$ with scalar sensor shifts
$m_{\mathrm{PRE}}(\tilde{t})$	EmSFMNN pretrained on PRE data set with wavelength dependent $\tilde{t}$
$m_{\mathrm{SEL}}(\tilde{t})$	EmSFMNN finetuned on SEL data set with $\tilde{t}$
$m_{\mathrm{CKA}}(\tilde{t})$	EmSFMNN finetuned on CKA data set with $\tilde{t}$
$m_{\mathrm{SEL}}(t)$	EmSFMNN finetuned on SEL data set with emulator t

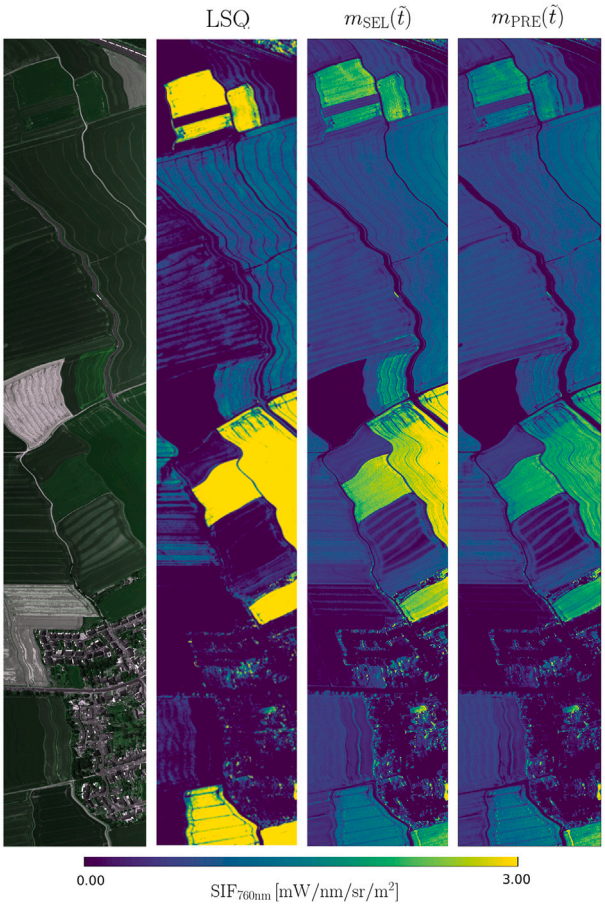

Fig. 4. Prediction example of a HyPlant acquisition recorded on 2018/07/26 15:30 CEST in Selhausen. Shown are a pseudo-color image (red: 682 nm, green: 700 nm, blue: 670 nm) (left), SIF estimate with $m_{\mathrm{SEL}}(\tilde{t})$ (center) and with $m_{\mathrm{PRE}}(\tilde{t})$ (right). (For interpretation of the references to colour in this figure legend, the reader is referred to the web version of this article.)

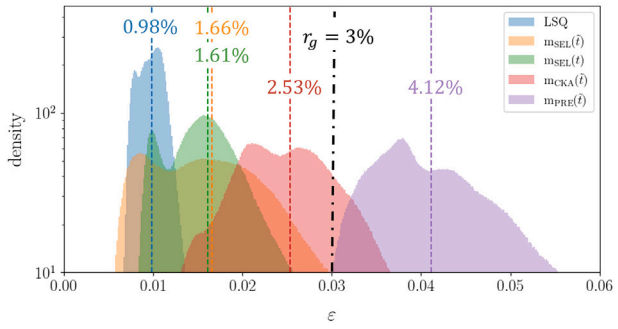

Fig. 5. Distribution of relative reconstruction errors ε (see Eq. 8) plotted logarithmically for different EmSFMNN set-ups as well as a least-squares optimization (LSQ) (see Table 4) in a HyPlant acquisition recorded on 2018/07/26 15:30 CEST in Selhausen (see Fig. 4). The median values of these distributions are reported directly in the figure with vertical lines. Mean relative reconstruction errors for $m_{\mathrm{SEL}}\mathrm{t}$ and $m_{\mathrm{SEL}}(\tilde{t})$ overlap in this figure. r_g denotes the relative uncertainty of the radiometric calibration.

data acquisition. However, its performance is close to what can be expected from the relative uncertainty of the radiometric calibration of the at-sensor radiance r_g. Since $m_{\mathrm{CKA}}(\tilde{\imath})$ (that has been finetuned on the CKA-2020 data set) is applied here on an acquisition from the SEL-2018 data set, effects due to different yearly calibrations can affect the reconstruction performance.

Finally, to assess the impact of finetuning it can be observed that the relative reconstruction error of $m_{\mathrm{PRE}}(\tilde{\imath})$ is constrained in the range 3–6 %. It is thus larger than the errors attributed purely to calibration uncertainties and indicates that the backbone PRE is not able to reconstruct the model at-sensor radiance of arbitrary HyPlant acquisitions from its learned feature representation without prior finetuning.

4.2. Validation with FLOX data

We validate EmSFMNN SIF predictions with top-of-canopy iFLD SIF estimates derived from radiance data recorded by FLOX devices. To be consistent with the FLOX iFLD retrieval yielding our ground-truth, we use the Gaussian fluorescence model assumption implemented in the simulations to calculate SIF_{760}. Five measurement time series are at our disposal acquired during HyPlant overflights in field campaigns in the years 2018–2021 (see Fig. 6). To support our comparison, we also report the validation results for three baseline methods that were adapted to hyperspectral HyPlant imagery (iFLD (Wieneke et al., 2016; Damm et al., 2014), SFM (Cogliati et al., 2019, 2015) and SFMNN (Buffat et al., 2025a)). Additionally, we show the impact of the emulator formulation and the finetuning on the performance of the standard training setup denoted by EmSFMNN($\tilde{\imath}$) in Table 5. To this end, we report (i) results for the EmSFMNN setup using the polynomial interpolation without band-wise sensor characterization, denoted as EmSFMNN($\imath$), and (ii) the performance of the coarsely pretrained SIF predictor, denoted as PRE (see Table 5).

We find that the EmSFMNN($\tilde{\imath}$) predictors finetuned to individual data sets generally are among the best SIF retrieval methods in terms of the mean absolute error with respect to FLOX estimates (MAE) and normalized MAE (nMAE) (defined as mean relative absolute errors as in Eq. 8). EmSFMNN($\tilde{\imath}$) yields MAE scores consistently smaller than 0.4 mW nm^{-1} sr^{-1} m^{-2} whereas stronger variation in MAE can be found in the case of the iFLD, SFM and SFMNN SIF predictions. We notably find a reduced overestimating bias of EmSFMNN as compared to SFMNN in Fig. 6 and a higher accuracy than in SFM and iFLD predictions.

Both the use of $\tilde{\imath}$ instead of $\imath$ and the finetuning considerably decrease the MAE. This can be concluded from the improved performance of EmSFMNN($\tilde{\imath}$) over EmSFMNN($\imath$) and PRE. These two aspects have been introduced to improve the model representation by (i) a more accurate simulation layer in the reconstruction loss and (ii) a more precise fitting of the spectral data by specializing the network weights to a selection of HyPlant lines. While the use of the non-specialized pretrained EmSFMNN model PRE leads to validation results comparable to the baseline methods, it is necessary to make use of a finetuning step to improve over the baseline methods iFLD, SFM and SFMNN.

In Table 5 we equally report the Pearson correlation scores r and the Explained Variance Score R^2. A consistent cross-validation assessment based on r and R^2 is, however, not possible throughout all validation data sets due to strongly variable performance under these two metrics. Due to the small number of validation data points these performance metrics are subject to large uncertainties. A reduced performance of EmSFMNN ($\tilde{\imath}$) in terms of r with respect to SFMNN is, however, observable in all data sets where such a comparison can be made. We hypothesize that this may be due to the stricter modelling approach of EmSFMNN resulting in a higher sensitivity to sensor noise. Finally, we point out that we find a consistent prediction underperformance in the WST-2019 dataset across all tested SIF retrieval algorithms in terms of r. In the cases exhibiting the highest accuracy scores (EmSFMNN($\tilde{\imath}$) and SFMNN) a negative and a non-significant correlation score r can be found. While we are unable to establish the reason for this behaviour, we hypothesize that it is partly explained by the overall variation in SIF across the WST-2019 dataset ($\sim 1.75 \pm 0.25$ mW nm^{-1} sr^{-1} m^{-2}) which is lower than the average estimated uncertainty of the analysed SIF estimators. In this case small errors have a large impact on the correlation. Secondly, dataset-specific effects leading to SIF dynamic prediction failure might be at play in all cases except SFM.

4.3. Topography

The emulator was derived from simulations covering an h_{gnd} range of 0–0.76 km and of h_{agl} 0.2–2.86 km. This allows the application of EmSFMNN predictors in acquisitions with large height variation where both the surface height h_{gnd} and flight height above ground level h_{agl} change significantly over the course of a single datatake. To test the reconstruction performance of EmSFMNN predictors under these circumstances we examine the TOPO data set consisting of HyPlant acquisitions with strong topographic variation and a nominal flight height of 600 m (see Table 1). We apply (i) the EmSFMNN predictor finetuned to the CKA-2020 (600 m) data set (denoted as m_{CKA}) and (ii) an EmSFMNN finetuned to the TOPO data set (m_{TOPO}). The finetuning of the m_{TOPO} and m_{CKA} was performed on the TOPO data set as described above (cf. Table 1) and only differed in the finetuning data set. Both predictors derive from an EmSFMNN backbone trained on the PRE data set which includes the data contained in TOPO. By examining on TOPO with both m_{CKA} and m_{TOPO} we can evaluate the importance of topography related distribution differences between finetuning data sets.

In Fig. 7(a) and (b) we summarize the residual statistics of m_{CKA} and m_{TOPO} as a function of the flight height h_{agl} in the full prediction spectral window $\mathcal{W}$ (750–770 nm) as well as in a narrow spectral window $\mathcal{W}_{\mathrm{O_2\ A}}$ in the O_2-A absorption band (759.5–761 nm). m_{CKA} outperforms the finetuned m_{TOPO} in $\mathcal{W}$ exhibiting a residual distribution with fewer outliers. Notably, m_{CKA} outperforms m_{TOPO} including in h_{agl} ranges that are not covered by the CKA-2020 (600 m) finetuning data set. The finetuning to the validation data set TOPO yields, however, to an improved m_{TOPO} performance in the O_2-A band with m_{TOPO} exhibiting an improved reconstruction performance overall. The strong reconstruction residual outliers of m_{TOPO} are consequently contained in spectral regions outside the O_2-A band as can be understood from the fact that its performance on $\mathcal{W}_{\mathrm{O_2\ A}}$ is less affected by it.

While we are able to assess the reconstruction performance of m_{TOPO} and m_{CKA}, we cannot evaluate the SIF predictions in the TOPO dataset due to lacking in-situ data. Therefore, we test whether in addition to the reconstruction performance the SIF prediction and reflectance estimation are independent of the h_{agl} variation. Fig. 8(a) shows that the SIF predictions of m_{TOPO} and m_{CKA} have a constant mean over most of the covered height range. This is to be expected in the case of a homogeneous distribution of fluorescence emitting surfaces. The decoupling of h_{agl} from the SIF prediction is only invalid in the range $h_{\mathrm{agl}} < 0.5$ km where both m_{TOPO} and m_{CKA} have a larger mean SIF prediction than in the rest of the height range. There are however significantly less HyPlant pixels falling in this range such that the homogeneity assumption is weakened due to a decreased statistical relevance.

In Fig. 9 we show an exemplary HyPlant acquisition that highlights the independence of the achieved SIF prediction and the reconstruction performance from h_{agl}. Both SIF and the fractional residual $\Delta L / L_{\mathrm{HyP}}$ are unaffected by the topographic variation along-track over the hill slope in the image center. The SIF predictions differ only slightly in m_{TOPO} and m_{CKA} due to differences in the finetuning training data set.

Concluding, we can observe that the influence h_{agl} on EmSFMNN's reconstruction performance, SIF and reflectance prediction is small. The variation of reconstruction errors, SIF and reflectance of both m_{TOPO} and

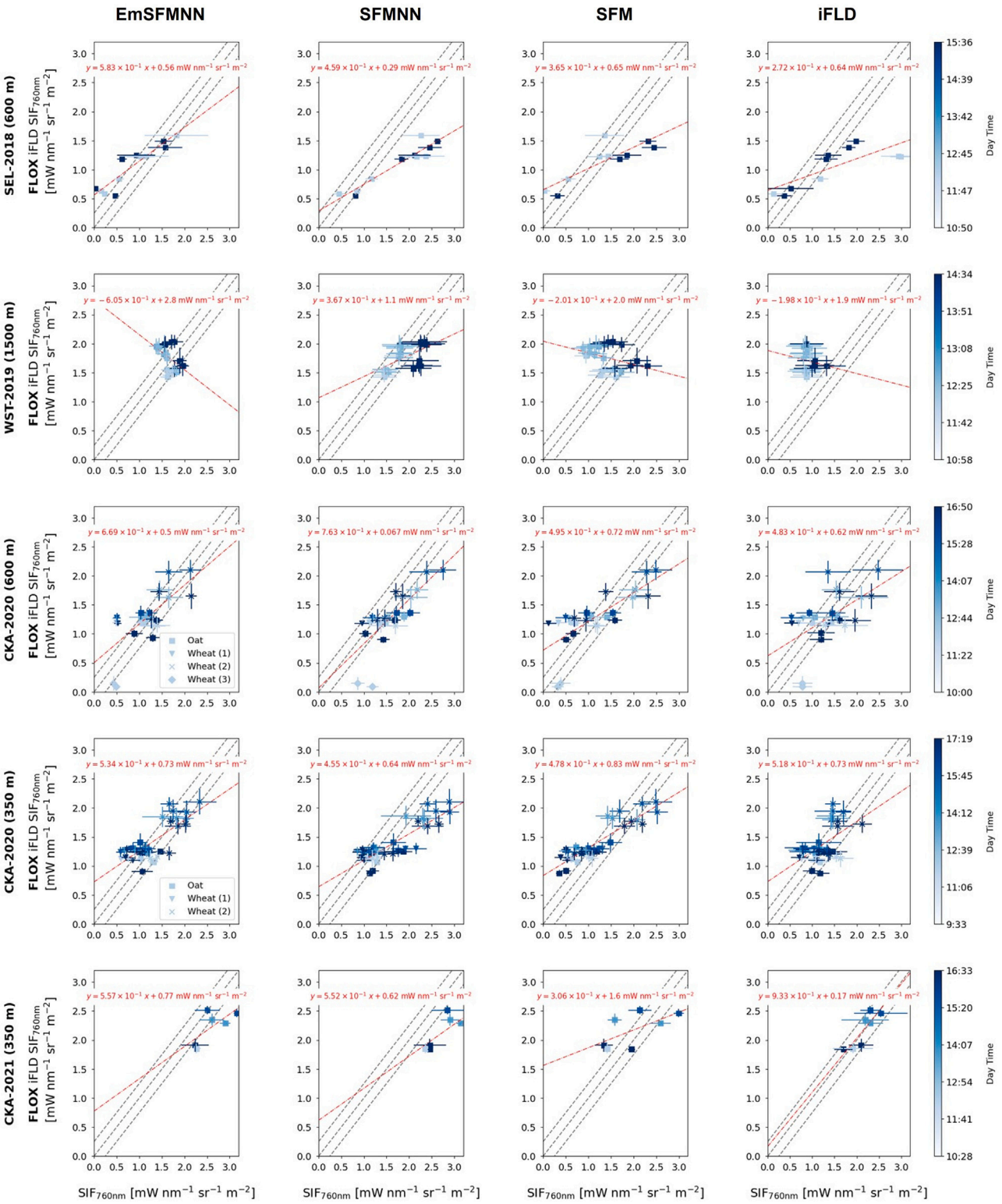

Fig. 6. FLOX-derived iFLD SIF vs. HyPlant-derived EmSFMNN, SFMNN, SFM and iFLD SIF in the five in-situ validation data sets (see Table 1). The dashed line and the red floating labels report the linear relationship between airborne and in-situ FLOX iFLD estimates. In the CKA-2020 data sets FLOX measurements from different devices are reported separately. The x-axes of the subplots are shared and labelled at the bottom. (For interpretation of the references to colour in this figure legend, the reader is referred to the web version of this article.)

m_{CKA} do not vary systematically with h_{agl}. It could be observed that the choice of the training dataset for finetuning had a larger effect on EmSFMNN's reconstruction performance than the topographic variation. This indicates that EmSFMNN can compensate for the variability in the atmospheric transfer with the specific choice of RTM emulation adopted in this contribution.

Table 5
Comparative validation of SFM, iFLD, SFMNN and EmSFMNN retrieval methods. We report the mean absolute error (MAE) of the EmSFMNN predictions with respect to FLOX measurements, the Pearson correlation r, the Explained Variance Score R^2, the normalized MAE (nMAE) defined as in Eq. (8) and the number of validation measurements N. In cases where the p-value of r is larger than 5 % we do not report r and write − instead. Similarly, in cases where $R^2 \leq 0$ we do not report R^2 and write −.

		r	R^2	MAE [mW nm^{-1} sr^{-1} m^{-2}]	nMAE	N
SEL-2018 (600 m)	EmSFMNN ($\tilde{t}$)	0.91	0.55	**0.26 ± 0.09**	**0.30**	10
	EmSFMNN (t)	0.86	**0.74**	0.46 ± 0.05	0.41	10
	PRE	0.78	0.57	0.47 ± 0.06	0.48	10
	SFMNN	**0.98**	–	0.68 ± 0.07	0.59	10
	SFM	0.96	–	0.51 ± 0.07	0.54	10
	iFLD	0.64	0.10	0.88 ± 0.00	0.69	11
WST-2019 (1500 m)	EmSFMNN ($\tilde{t}$)	**−0.54**	–	**0.29 ± 0.05**	0.16	15
	EmSFMNN (t)	−0.73	–	1.48 ± 0.05	0.88	15
	PRE	−0.78	–	0.41 ± 0.04	0.22	15
	SFMNN	–	–	**0.22 ± 0.10**	**0.12**	15
	SFM	–	–	0.53 ± 0.08	0.30	15
	iFLD	–	–	0.80 ± 0.10	0.45	15
CKA-2020 (600 m)	EmSFMNN ($\tilde{t}$)	0.65	0.02	**0.35 ± 0.05**	0.54	16
	EmSFMNN (t)	0.69	0.18	0.47 ± 0.05	0.56	16
	PRE	0.67	–	0.39 ± 0.06	**0.48**	16
	SFMNN	0.69	**0.34**	**0.33 ± 0.06**	0.99	16
	SFM	**0.72**	–	0.48 ± 0.06	0.53	16
	iFLD	0.64	–	0.42 ± 0.09	0.70	16
CKA-2020 (350 m)	EmSFMNN ($\tilde{t}$)	0.74	0.04	**0.28 ± 0.04**	0.22	34
	EmSFMNN (t)	0.81	**0.12**	0.35 ± 0.04	0.27	34
	PRE	0.80	–	0.33 ± 0.04	0.25	34
	SFMNN	0.84	–	0.34 ± 0.04	0.24	34
	SFM	**0.87**	–	0.35 ± 0.04	0.27	34
	iFLD	0.58	0.05	**0.28 ± 0.05**	**0.20**	34
CKA-2021 (350 m)	EmSFMNN ($\tilde{t}$)	–	0.19	0.38 ± 0.09	**0.17**	6
	EmSFMNN (t)	–	0.16	1.07 ± 0.12	0.49	6
	PRE	–	0.30	0.70 ± 0.09	0.32	6
	SFMNN	–	–	0.65 ± 0.10	0.29	6
	SFM	–	–	0.50 ± 0.08	0.23	6
	iFLD	**0.85**	**0.71**	**0.12 ± 0.18**	0.18	6

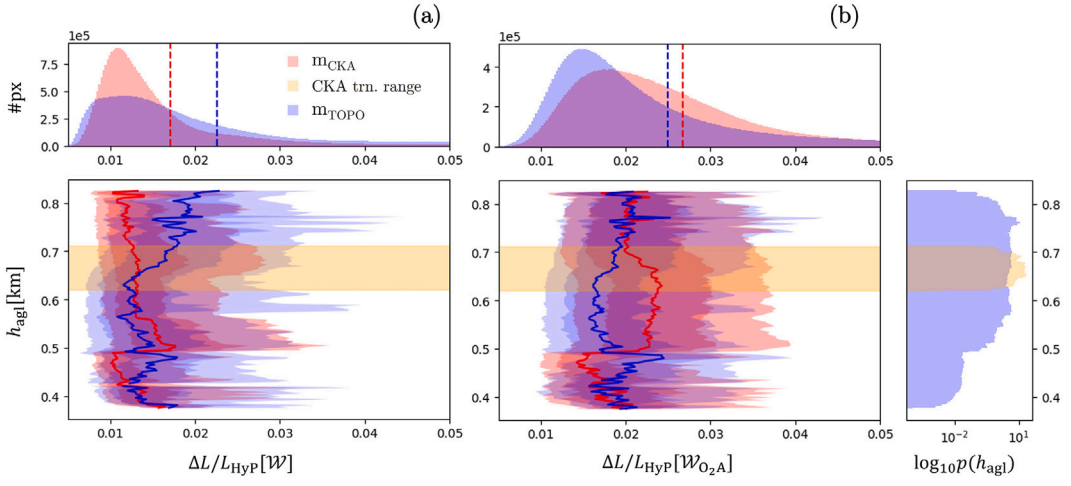

Fig. 7. Top row: Marginalized distribution of relative reconstruction residuals of m_{CKA} in red and m_{TOPO} in blue in the whole fitted spectral window $\mathcal{W}$ (a) and in the spectral window $\mathcal{W}_{O_2\ A}$ in the O_2-A band (b). Bottom left: Relative reconstruction residuals of m_{CKA} (red) and m_{TOPO} (blue) stratified by the sensor height above ground h_{agl} in $\mathcal{W}$ (a) and $\mathcal{W}_{O_2\ A}$ (b). Red and blue lines denote the means, dark areas denote the 25–75 percentile ranges, light areas denote the 10–90 percentile ranges. In yellow we highlight the range of h_{agl} covered by the CKA-2020 data set on which m_{CKA} was finetuned. Bottom right: Logarithmic empirical histogram of h_{agl} of CKA-2020 in yellow and TOPO in blue. (For interpretation of the references to colour in this figure legend, the reader is referred to the web version of this article.)

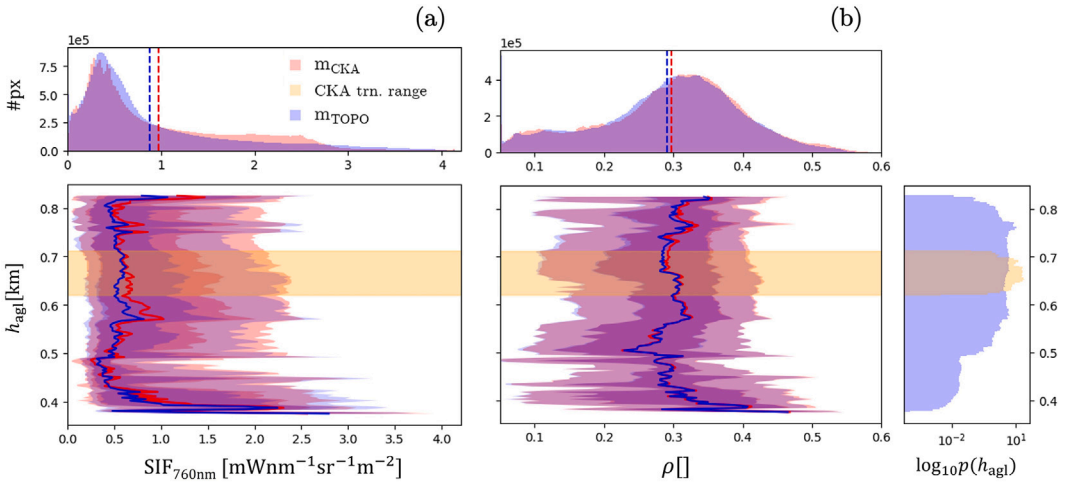

Fig. 8. Top row: Marginalized distribution of reflectance offset parameter ρ (a) and fluorescence emission amplitude F_{737} as predicted by m_{CKA} in red and m_{TOPO} in blue. Bottom left: reflectance offset parameter ρ (a) and fluorescence emission amplitude F_{737} (b) stratified by the sensor height above ground h_{agl} as predicted by m_{CKA} in red and by m_{TOPO} in blue. Red and blue lines denote the means, dark areas denote the 25–75 percentile ranges, light areas denote the 10–90 percentile ranges. In yellow we highlight the range of h_{agl} covered by the CKA-2020 data set on which m_{CKA} was finetuned. Bottom right: Logarithmic empirical histogram of h_{agl} of CKA-2020 in yellow and TOPO in blue. (For interpretation of the references to colour in this figure legend, the reader is referred to the web version of this article.)

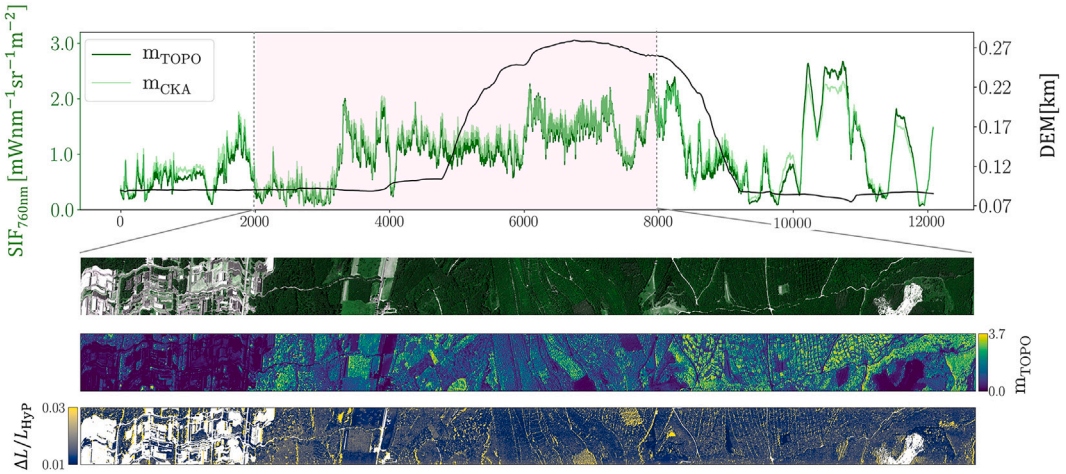

Fig. 9. Top row: Shown are the SIF prediction of TOPO(1) and CKA(1) along the ground surface altitude h_{gnd} derived from a matching Digital Elevation Map (DEM). Lower rows: shown are a false color image of the HyPlant at-sensor radiance, the pixelwise $SIF_{760\ nm}$ prediction of TOPO (given in mW nm^{-1} sr^{-1} m^{-2}) and the relative reconstruction error of TOPO in the spectral window $\mathcal{W}$ in a subset of the HyPlant acquisition displayed in the top row. (For interpretation of the references to colour in this figure legend, the reader is referred to the web version of this article.)

5. Discussion

5.1. Simulation and emulator design and limitations

In this work the integrated use of a polynomial emulator and self-supervised neural network training could be shown to yield both fast and accurate estimation of SIF at 760 nm. Two design choices of the simulation model are of particular relevance to the discussion of EmSFMNN's performance.

Firstly, the model underlying the simulation tool and the emulator was set up to exclude cross-correlations between input parameters. While such cross-correlations may be learnt in EmSFMNN's training setup, we do not implicitly enforce these by, e.g., making use of a physiologically plausible model such as SCOPE (Tol et al., 2009a). Such relationships would have confounded EmSFMNN's capacity to fit the at-sensor radiance signal purely on the basis of physical principles. As an example, it is well known that both the reflectance in the spectral region of photosynthetically active radiation (PAR) and the total fluorescence emission amplitude F_{737} are strongly correlated in green vegetation due to a common dependency on leaf chlorophyll concentration (Verrelst et al., 2015). Reconstructed SIF products involving spaceborne reflectance products such as the MODIS-based RSIF (Gentine and Alemohammad, 2018) and RTSIF (Chen et al., 2022), reconstructing the TROPOMI SIF product, make use of this relationship. Detailed studies with field data could also establish cross-correlations in reflectance-based features and top-of-canopy SIF derived from airborne platforms resulting from structural effects (Yang and Van Der Tol, 2018; Yang et al., 2019) and biochemical processes related to non-photochemical quenching (Pinto et al., 2020). However, such dependencies, if incorporated a-priori in the predictor modelling assumptions, are prone to lead to model bias and, importantly, may well induce larger gradients in the self-supervised loss than the small at-sensor fluorescence signal. As a consequence, the influence of such fixed correlations on

the feature-based optimization and ultimately on the SIF estimate may trump the physical and causal spectral reconstruction approach leveraged in EmSFMNN.

Secondly, this contribution has focused on SIF retrieval in a narrow spectral range. The spectral range around the O_2-A absorption band of the simulation database has allowed us to (1) parameterize the reflectance and fluorescence with simple functions (second-order polynomial, Gaussian) and (2) use a polynomial model to approximate the simulation database. The polynomial form chosen for the emulator was advantageous to the EmSFMNN setup as it allowed an easy integration of the emulator in the neural network architecture: both forward pass and backward gradient computation were achieved by implementing the emulator as a fixed linear layer.

The use of the plain polynomial emulator t (Pato et al., 2023, 2024) for EmSFMNN has led to subpar performance with respect to in-situ FLOX measurements. While the lack of spectrally explicit sensor characterization did not lead necessarily to decreased performance in terms of spectral reconstruction residuals, the emulator model's incompleteness has caused systematic errors in the signal decomposition. As a consequence, we have implemented an emulator capable of simulating HyPlant at-sensor radiances with bandwise spectral shifts with an efficient approximation $\tilde{t}$. This approximation can be shown to yield acceptable relative errors peaking at ~3.5 % with respect to the exact, but computationally demanding emulator solution (see Appendix B). The error incurred by the approximation in the O_2-A absorption band may, however, still be significant in terms of reconstruction accuracy considering that the mean fluorescence emission at 760 nm in HyPlant acquisition amounts also to < 3 % of the mean at-sensor signal. The validation of the SIF prediction of EmSFMNN models integrating this approximate emulator $\tilde{t}$ proved sufficient to outperform all baseline methods in terms of accuracy.

While we have shown the application of EmSFMNN to HyPlant FLUO data in this contribution, the EmSFMNN approach to retrieve SIF can be implemented for data from different imaging sensors (e.g., in DESIS (Buffat et al., 2025b)) and could be extended to other spectral regions (e.g., the O_2-B band). Since the network architecture interacts with the data in the loss only through the interface of the emulator representing the physical constraints of the retrieval problem, such a change in the data modality would simply necessitate adapting the emulator. In particular, the modelling of the sensor in the simulation tool (Pato et al., 2025) and an extension of the reflectance and fluorescence parametric functions to the new spectral range would be required. Further research in emulator representations of simulated hyperspectral at-sensor radiance including bandwise sensor characterization is thus warranted. While the simple polynomial approach adopted here was suitable for the spectral range and simulation model that had been fixed for the EmSFMNN O_2-A SIF retrieval problem on HyPlant data, the integration of different emulator architectures (Verrelst et al., 2016, 2017; Bue et al., 2019) may become necessary for retrieval in different data modalities.

Finally, an extension of EmSFMNN to a generalized set of hyperspectral imaging sensors would equally require analysis of EmSFMNN's prediction performance under variable sensor noise distributions. In this work, the simulation model underlying the emulation of the atmospheric radiative transfer did not include sensor- or observation-specific noise distributions. An overall increased uniform noise level (decrease of the sensors signal-to-noise ratio) would decrease the quality of the gradients deduced from the reconstruction loss and hence would affect EmSFMNN's prediction performance negatively. More importantly, EmSFMNN's training setup would be particularly impacted by spectrally non-uniform noise patterns as these would result in biased estimates of the model parameters in the presented training setup.

5.2. Prediction of atmospheric variables

We have tested the quality of EmSFMNN's signal decomposition with respect to its reconstruction performance and the agreement of its SIF prediction with in-situ measurements. We could not validate the accuracy of the predicted atmospheric variables (water vapour content H_2O and aerosol optical thickness AOT_{550}) with direct measurements. The prediction of these variables is understood to be very challenging in the setting adopted in the presented retrieval method since (i) the sensitivity of the at-sensor radiance to water vapour and AOT_{550} in the fitting spectral window (750–770 nm) is small (Pato et al., 2025), (ii) the variation of both parameters in the training data is expected to be small due to similar meteorological conditions during HyPlant campaigns. Furthermore, there may be remaining representation insufficiencies of the emulator t that can result in EmSFMNN predictors leveraging the degrees of freedom in these parameters to adjust the atmospheric estimate to the observational data. In particular, we highlight that the at-sensor radiance simulations all have used a standardized atmospheric pressure profile (MODTRAN *mid-latitude summer*) while we have not adapted the emulator to the meteorological conditions at acquisition time. Thus, while H_2O and AOT_{550} were included explicitly in the simulations and EmSFMNN addresses these parameters with a spatial constraint, accurate retrieval of these parameters cannot be expected.

We show in Fig. 10, however, that the distributions of AOT_{550} estimates of single HyPlant acquisitions are approximately consistent with AOT_{550} measurements of a CIMEL instrument located at the JOYCE AERONET station (FZJ-JOYCE, 2024) nearby the geographical center of HyPlant acquisitions in the SEL-2018 data set (~5 km). We gathered CIMEL for this analysis CIMEL AOT_{550} measurements with a maximum time difference to the HyPlant acquisition time of 20 min. In particular, we find a strong decrease in AOT_{550} on 2018/06/27 which is reflected in EmSFMNN estimates as well. Furthermore, MODIS Terra and Aqua AOT_{550} estimates from data with a maximum two-hour time difference to the HyPlant acquisition are similar to EmSFMNN. The MODIS estimates exhibit large uncertainties, however, such that they must be considered to gauge only very roughly the accuracy of EmSFMNN AOT_{550}.

A more detailed study of parameters pertaining to the atmospheric composition at acquisition time would be of relevance for EmSFMNN if it were to be applied to more susceptible spectral regions covered by full-spectrum retrieval. Furthermore, more extensive analysis could establish the performance benefit of including atmospheric estimates from different sensors as in (Buffat et al., 2025b). Since such a procedure is planned with the FLEX/Sentinel-3 tandem orbit configuration (Drusch et al., 2017), such analysis is especially relevant for further work on the application of EmSFMNN on FLEX data.

5.3. Feature generalization of EmSFMNN

The validation analyses have shown good performance of EmSFMNN models on data for which the models were not finetuned. In Section 4.1 we could show that $m_{CKA}(\tilde{t})$ applied to a HyPlant acquisition from SEL-2018 yielded a mean reconstruction performance of $\epsilon < 3.15$ % as compared to the result of the finetuned $m_{SEL}(\tilde{t})$ of $\epsilon < 2.31$ %. The SEL-2018 data set is similar to CKA-2020 on which $m_{CKA}(\tilde{t})$ was finetuned. Both data sets cover predominantly agricultural fields and exhibit only a small fraction of forested areas such that $m_{CKA}(\tilde{t})$ and $m_{SEL}(\tilde{t})$ are trained with a similar spectral surface composition. Furthermore, the h_{agl} and h_{gnd} ranges in both data sets are overlapping. However, the data sets were acquired in different years resulting in varying radiometric sensor calibrations associated with a mean uncertainty of 3 %. These results indicate that EmSFMNN generalizes well across HyPlant data sets with large similarities. In addition, Section 4.2 could establish that the non-finetuned backbone predictor PRE could estimate SIF outperforming the SFM, iFLD and SFMNN baselines in some validation data sets, highlighting the impact of strong feature generalization on EmSFMNN SIF estimates.

Furthermore, generalization capability of EmSFMNN across topographic changes could be established in Section 4.3. We could show that $m_{CKA}(\tilde{t})$, which was finetuned on data exhibiting only small

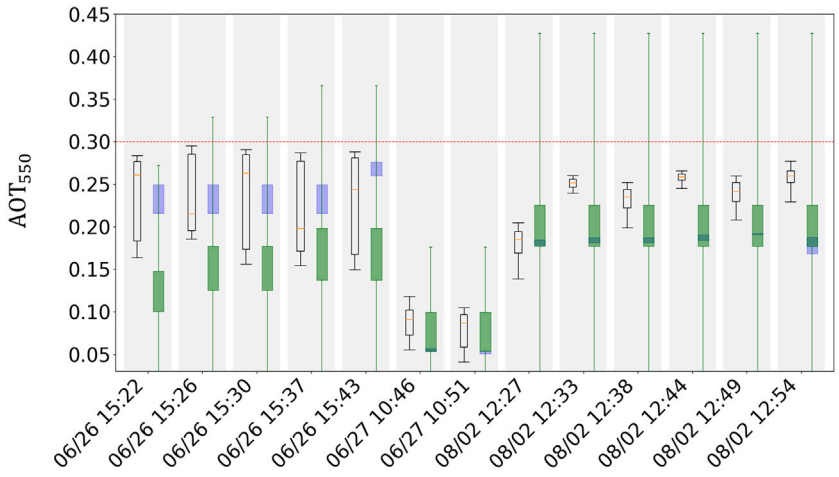

Fig. 10. Comparison of AOT_{550} estimates. *Black*: distribution of EmSFMNN AOT_{550} estimates in single HyPlant acquisitions, box width show 25–75 % percentiles and whiskers show 5 – 95 % percentiles, the median is reported in orange, *Blue*: CIMEL measurements of the JOYCE AERONET station (FZJ-JOYCE, 2024) located at ~5 km from the SEL-2018 HyPlant acquisitions (left), box width shows the standard deviation of all measurements recorded within 20 min of the HyPlant acquisition time, *Green*: Deep Blue AOT_{550} products of MODIS Terra (MODIS Atmosphere Science Team, 2017a) and Aqua (MODIS Atmosphere Science Team, 2017b) at 10 km resolution, box width shows the standard deviation of available Terra and Aqua products within two hours of the HyPlant acquisition time and the whiskers represent the mean of the provided uncertainty of the estimates within a 30 km window around the location of the CKA-2020 estimates. *Red*: maximum AOT_{550} covered in simulation database. (For interpretation of the references to colour in this figure legend, the reader is referred to the web version of this article.)

topographic variation, had an improved reconstruction performance over an EmSFMNN instance that was finetuned on the full topographic range present in TOPO. We interpret this finding such that the learned feature space successfully disentangles features that are unrelated to the topographic change and the associated optical path length differences (i.e. the reflectance and SIF emission). This in turn is corroborated by the observation that both the statistical distribution of the predicted SIF emission and of the reflectance are constant across the full topographic range.

The possibility to base the inference of SIF in new data on a single generalized SIF retrieval model is an advantage of the feature based optimization of EmSFMNN over other physical SIF retrieval methods for which a repeated pixelwise or campaign-wise optimization has to be conducted. While we have not conducted validation studies on completely new data sources, that were not included in the pretraining or finetuning training data, we could show that the EmSFMNN could be finetuned successfully to a range of HyPlant data sets without complete retraining. If the importance of finetuning on the SIF prediction performance could be better quantified and reduced, the emulator based SIF retrieval method developed here could therefore prove to be a useful contribution to efficient SIF retrieval method for hyperspectral high-throughput imaging sensors where inference speed is critical.

6. Conclusion

In this work, we have applied EmSFMNN to HyPlant FLUO data. This novel emulation-based SIF retrieval method was first presented by Buffat et al. (Buffat et al., 2025b) on DESIS acquisitions. EmSFMNN utilizes feature-based optimization and hyperspectral RTM emulation to disentangle the fluorescence signal from the at-sensor radiance. We have proposed an extension to the originally purely polynomial model used for DESIS to represent spectrally explicit CW and FWHM shifts in HyPlant computationally efficiently. This has allowed for the training of EmSFMNN on a significant fraction of the total available HyPlant acquisitions.

The direct SIF validation with in-situ SIF estimates derived from FLOX measurements has shown that the accuracy of finetuned EmSFMNN outperforms both SFMNN and traditional baseline methods (SFM, iFLD). Importantly, we could also show that a pretrained backbone EmSFMNN predictor generalized well across the considered HyPlant campaigns such that improved EmSFMNN SIF retrievals could be achieved at a smaller computational cost than traditional pixel-wise optimization. The computational efficiency of this approach is due to the feature-based nature of EmSFMNN that allows a single model to be used for inference without prior finetuning.

Furthermore, in an analysis with HyPlant acquisition with strong topographic variability, we demonstrated that the setup allows for a generalization of the application domain of SIF retrieval. The possibility to constrain the retrieval by exact topography and geometrical information has allowed the application of EmSFMNN to HyPlant acquisitions with strong topographic variation where prior retrieval algorithms could not be applied in a straightforward fashion.

Finally, we have presented a small comparison of EmSFMNN predicted AOT_{550} with high-fidelity CIMEL AOT_{550} measurements in a single campaign data set consisting of 13 acquisitions giving first insights into the accuracy of the atmospheric characterization estimated by EmSFMNN. We found a consistent variation of predicted AOT_{550} with the measurements which supports the hypothesis that the disentangling of reflectance, fluorescence and atmospheric components as predicted by EmSFMNN is trustworthy. Further work is, however, necessary to assess EmSFMNN's performance in predicting secondary atmospheric components under general observation conditions.

As HyPlant FLUO is the airborne demonstrator for the spaceborne FLORIS sensor, that will be operated onboard ESA's Earth Explorer mission, this work is relevant for further research in computationally efficient SIF retrieval algorithms for data acquired by FLORIS. While (Buffat et al., 2025b) have shown how EmSFMNN could be applied to radiance data acquired on a spaceborne platform, in this work we have focused specifically on the requirements of HyPlant FLUO, a sensor comparable to FLORIS. The encouraging results in terms of precision in both DESIS and HyPlant FLUO suggest that EmSFMNN may be successfully applied to FLORIS data as well.

CRediT authorship contribution statement

Jim Buffat: Writing – review & editing, Writing – original draft, Visualization, Validation, Software, Methodology, Investigation, Formal analysis, Data curation, Conceptualization. **Miguel Pato:** Writing – review & editing, Supervision, Project administration, Funding acquisition, Data curation, Conceptualization. **Kevin Alonso:**

Conceptualization. **Stefan Auer:** Writing – review & editing, Project administration, Funding acquisition, Conceptualization. **Emiliano Carmona:** Writing – review & editing, Conceptualization. **Stefan Maier:** Writing – review & editing, Supervision, Conceptualization. **Rupert Müller:** Conceptualization. **Patrick Rademske:** Data curation. **Uwe Rascher:** Writing – review & editing, Supervision, Project administration, Funding acquisition, Conceptualization. **Hanno Scharr:** Writing – review & editing, Supervision, Project administration, Methodology, Funding acquisition, Conceptualization.

Declaration of competing interest

The authors declare the following financial interests/personal relationships which may be considered as potential competing interests:

Jim Buffat, Miguel Pato, Kevin Alonso, Stefan Auer, Emiliano Carmona and Rupert Müller report that financial support was provided by the Helmholtz Artificial Intelligence Cooperation Unit. If there are other authors, they declare that they have no known competing financial interests or personal relationships that could have appeared to influence the work reported in this paper.

Acknowledgements

This work is part of the project “FluoMap” (Impulsfonds-Förderkennzeichen ZT-I-PF-5–12) funded by the Helmholtz Initiative and Networking Fund, Helmholtz AI, Deutsches Zentrum für Luft- und Raumfahrt (DLR) and Forschungszentrum Jülich GmbH (FZJ). The authors gratefully acknowledge computing time on the supercomputer JURECA (Supercomputing Centre, 2021) at Forschungszentrum Jülich under grant no. fluomap-ct. We gratefully acknowledge the financial support by the European Space Agency (ESA) for airborne data acquisition and data analysis in the frame of the FLEXSense campaign (ESA Contract No. 4000125402/ 18/NL/NA) and the Photoproxy project (ESA Contract No. 4000125731/19/NL/LF). Additionally, HyPlant and FLOX data acquisition have partially been funded by the German Federal Ministry of Education and Research within the German-Plant-Phenotyping Network (DPPN) (project identification number: 031A053), the ‘Strukturwandel-Projekt Bioökonomie REVIER’, which is funded by the German Federal Ministry of Education and Research (project identification number 031B0918A), the Deutsche Forschungsgemeinschaft (DFG, German Research Foundation) under Germany’s Excellence Strategy – EXC 2070–390732324 and the project Land Surface Interactions with the Atmosphere over the Iberian Semi-arid Environment (LIAISE) funded by the Centre national de la recherche scientifique (CNRS). Open access is funded by the Deutsche Forschungsgemeinschaft (DFG, German Research Foundation) – 491111487.

Appendix A. Emulation of a wavelength dependent sensor model

The simulation database is created for scalar shifts $\Delta\lambda$ and $\Delta\sigma$, i.e., simulated spectra $s(\vec{p}) \in \mathbb{R}^{\Lambda}$ will experience the same simulated sensor miscalibration in all wavelengths $\lambda \in \Lambda$. In a realistic sensor model, CW and FWHM shifts are, however, functions of the wavelength such that we ought to find an emulator with dependency on shifts $\vec{\Delta\lambda} \in \mathbb{R}^{\Lambda}$ and $\vec{\Delta\sigma} \in \mathbb{R}^{\Lambda}$ in addition to the other input parameters $\vec{p}$. We assume that there is no cross dependency of the shifts either in the measured at-sensor radiance L or the simulator L_s, i.e.,

$$\forall i \neq k : \ \frac{dL_i}{dv_k} = \frac{d\left(L_s\right)_i(\vec{p}, \vec{\Delta\lambda}, \vec{\Delta\sigma})}{dv_k} = 0, \ v \in \{\vec{\Delta\lambda}, \vec{\Delta\sigma}\}. \tag{A.1}$$

In this case a naive approach to extend the emulator could be achieved by rewriting

$$t_d^{\Lambda}\left(\vec{p}, \vec{\Delta\lambda}, \vec{\Delta\sigma}\right) = \left(t_d(\lambda_i \mid \vec{p}, \Delta\sigma_i, \Delta\lambda_i)\right)_{0 \leq i \leq \Lambda}, \tag{A.2}$$

where t_d is defined in Eq. (2). Since the simulation database covers a large number of spectral bands ($\Lambda = 349$) such an approach results in a significant increase in computation time for a single spectrum; the emulator would need to be run Λ times for a single emulated spectrum. We therefore adopt an approximation. We derive a multiplicative correction factor

$$b(\lambda_i \mid \vec{\Delta\lambda}, \vec{\Delta\sigma}) = \mathbb{E}\left[w\left(\lambda_i \mid \vec{p}, \Delta\lambda_i, \Delta\sigma_i\right)\right] \tag{A.3}$$

$$= \mathbb{E}\left[\frac{t_d\left(\lambda_i \mid \vec{p}, \Delta\lambda_i, \Delta\sigma_i\right)}{t_d\left(\lambda_i \mid \vec{p}, \Delta\lambda_i = \Delta\sigma_i = 0\right)}\right] \tag{A.4}$$

where the expectation is calculated by sampling randomly over the parameter distribution in the input parameter space. As we will show below, the variance over this distribution is very small, such that we can write

$$\tilde{t}_d\left(\lambda_i \mid \vec{p}, \vec{\Delta\lambda}, \vec{\Delta\sigma}\right) \approx b(\lambda_i \mid \vec{\Delta\lambda}, \vec{\Delta\sigma}) \cdot t_d\left(\lambda_i \mid \vec{p}, \Delta\lambda_i = \Delta\sigma_i = 0\right). \tag{A.5}$$

The fitting of b has only to be performed once prior to training. Thus, only the inference computation time is relevant and the time for fitting b can be neglected. With b being sufficiently simple we therefore can reduce the relevant computation cost by adopting $\tilde{t}_d$ over t_d^{Λ} (see Table B.6).

Table B.6
Prediction time measurements for the original emulator t_4, the original emulator applied in a bandwise fashion t_4^{Λ} and the emulator approximation $\tilde{t}_4$. In the case of t_4 only scalar sensor shifts were computed. The values represent the average of 20 time measurements on a single GPU (NVIDIA Quadro RTX 8000) predicting a batch of 10^4 samples.

	t_4	t_4^{Λ}	$\tilde{t}_4$
Prediction time per sample	0.28 μs	55.40 μs	1.93 μs

Appendix B. Accuracy of the extended emulation

We have trained a 4^{th} order polynomial emulator t on simulation databases covering the parameter ranges given in Table 2 as in (Pato et al., 2024). In order to allow for efficient training we then have implemented the emulator extension for wavelength dependent shifts $\tilde{t}$ (as defined in Appendix A) based on the polynomial emulator t_4 which acts only on scalar shifts as outlined in Section 3.3. To this end, we have computed the multiplicative factor m as the expectation in Eq. (A.3). To compute the distribution, we uniformly sampled a large number of parameter combinations $\vec{p}$ and sensor shifts $\vec{\Delta\lambda}$ and $\vec{\Delta\sigma}$ in the input space spanned by the individual parameter ranges.

We found the standard deviations of w to be bounded by 3.5 % under CW shifts and 0.06 % by FHWM shifts which we regarded as sufficiently small to approximate it by its mean m (see Fig. A.11). Subsequently, we fitted a 5th order polynomial to the derived m to gain a multiplicative factor defined on the whole input parameter space discarding the need for interpolation during prediction. The dimension of this polynomial was required to be just large enough to fit m well. The use of $\tilde{t}_4$ leads to a significant time reduction as compared to t_4^{Λ} (cf. Table B.6).

In order to evaluate the accuracy of $\tilde{t}$ we compared it to t_4^{Λ} on a uniformly sampled test set. While t_4^{Λ} takes significantly longer to compute, its accuracy with respect to the RTM is as high as the emulator itself since it essentially computes the emulator in a bandwise fashion. In Fig. B.12 we show that the mean relative error incurred by using the approximation $\tilde{t}_4$ is smaller than 1 %. However, the 95 % percentile reaches a relative error of 3.5 % inside the O_2-A band. We equally show the effect of neglecting bandwise shifts by comparing emulations of t_4^{Λ} with t_4 emulations leveraging only scalar shifts. The same parameters $\vec{p}$ were used for t_4^{Λ} and t_4 with only $\Delta\lambda$ and $\Delta\sigma$ set to a fixed scalar value for t_4. The relative errors can reach up to 10–20 % in the O_2-A band highlighting the importance of bandwise sensor characterization.

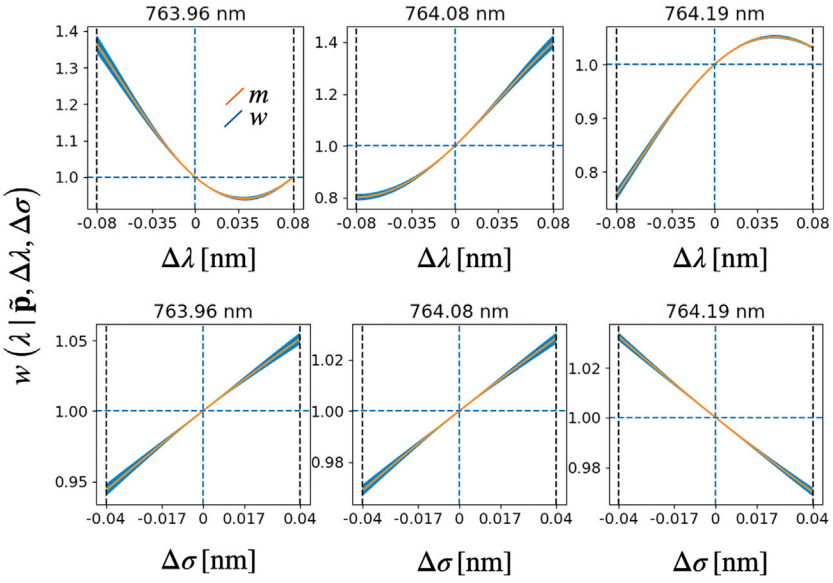

Fig. A.11. Multiplicative unitless factor w of t_4 under variable sensor shifts ($\Delta\lambda$ and $\Delta\sigma$) in three selected wavelengths. In blue is plotted the standard deviation of w (as defined in Eq. (A.3)) over the distribution of randomly sampled emulator parameter configurations $\vec{p}$. The fitted mean used as multiplicative correction b (see Eq. (A.3)) is plotted in orange. (For interpretation of the references to colour in this figure legend, the reader is referred to the web version of this article.)

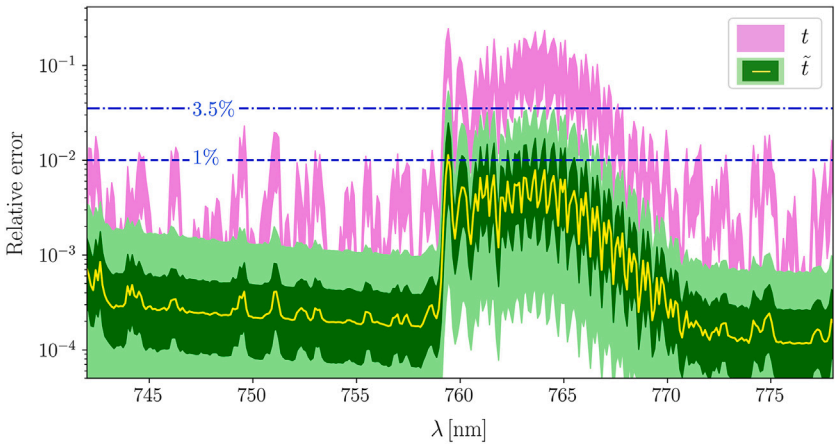

Fig. B.12. Logarithmically displayed relative errors of the approximate emulator $\tilde{t}_4$ (green/yellow) and scalar shift emulator t (pink) with respect to the accurate t_4^{Λ} emulator. In the case of t_4 we set $\Delta\lambda = \Delta\sigma = 0$. The 25−75 % percentile range is plotted in dark green, the 5 %–95 % percentile range in light green, the mean in yellow. Pink denotes the 25%–75 % percentile range. (For interpretation of the references to colour in this figure legend, the reader is referred to the web version of this article.)

Appendix C. Supplementary data

Supplementary data to this article can be found online at doi:10.1016/j.rse.2025.115203.

Data availability

Data will be made available on request.

References

Alonso, L., Gomez-Chova, L., Vila-Frances, J., Amoros-Lopez, J., Guanter, L., Calpe, J., Moreno, J., 2008. Improved Fraunhofer line discrimination method for vegetation fluorescence quantification. IEEE Geosci. Remote Sens. Lett. 5 (4), 620–624. https://doi.org/10.1109/LGRS.2008.2001180

Anderson, T.L., Charlson, R.J., Winker, D.M., Ogren, J.A., Holmén, K., 2003. Mesoscale variations of tropospheric aerosols*. J. Atmos. Sci. 60 (1), 119–136. https://doi.org/10.1175/1520-0469(2003)060{<}0119:MVOTA{>}2.0.CO;2.

Berk, A., Conforti, P., Kennett, R., Perkins, T., Hawes, F., van den Bosch, J., 2014. MODTRAN® 6: a major upgrade of the MODTRAN® radiative transfer code. In: 2014 6th Workshop on Hyperspectral Image and Signal Processing: Evolution in Remote Sensing (WHISPERS), pp. 1–4, https://doi.org/10.1109/WHISPERS.2014.8077573

Buffat, J., Pato, M., Alonso, K., Auer, S., Carmona, E., Maier, S., Müller, R., Rademske, P., Siegmann, B., Rascher, U., Scharr, H., 2025a. A multi-layer perceptron approach for SIF retrieval in the O_2-a absorption band from hyperspectral imagery of the hyplant airborne sensor system. Remote Sens. Environ. 318, 114596. https://doi.org/10.1016/j.rse.2024.114596

Buffat, J., Pato, M., Alonso, K., Auer, S., Carmona, E., Maier, S., Müller, R., Rademske, P., Rascher, U., Scharr, H., 2025b. Retrieval of sun-induced plant fluorescence in the o_2-a absorption band from DESIS imagery. In: Bue, A.D., Canton, C., Pont-Tuset, J., Tommasi, T. (Eds.), Computer Vision – ECCV 2024 Workshops. Springer, Nature Switzerland, Cham, pp. 81–100. https://doi.org/10.1007/978-3-031-91835-3_6

Buffat, J., Rascher, U., Rademske, P., Siegmann, B., Junker-Frohn, L.V., Emin, D., 2024a. HyData: HyPlant FLUO at-Sensor Radiance Data Packages and FLOX Measurements for SIF Retrieval Method Development from Selected Campaigns of the Years 2018–2023, https://doi.org/10.26165/JUELICH-DATA/QKJKPW

Buffat, J., Pato, M., Alonso, K., Auer, S., Carmona, E., Maier, S., Müller, R., Rademske, P., Rascher, U., Scharr, H., 2024b. Selected HyPlant, DESIS and OCO-3 Acquisitions for the Cross-Comparison of Sun-Induced Fluorescence Products, https://doi.org/10.26165/JUELICH-DATA/YNYLFQ

Bue, B.D., Thompson, D.R., Deshpande, S., Eastwood, M., Green, R.O., Natraj, V., Mullen, T., Parente, M., 2019. Neural network radiative transfer for imaging spectroscopy. Atmos. Meas. Tech. 12 (4), 2567–2578. https://doi.org/10.5194/amt-12-2567-2019

Cogliati, S., Verhoef, W., Kraft, S., Sabater, N., Alonso, L., Vicent, J., Moreno, J., Drusch, M., Colombo, R., 2015. Retrieval of sun-induced fluorescence using advanced spectral fitting methods. Remote Sens. Environ. 169, 344–357. https://doi.org/10.1016/j.rse.2015.08.022

Cogliati, S., Celesti, M., Cesana, I., Miglietta, F., Genesio, L., Julitta, T., Schuettemeyer, D., Drusch, M., Rascher, U., Jurado, P., Colombo, R., 2019 1840. A spectral fitting algorithm to retrieve the fluorescence spectrum from canopy radiance. Remote Sens. 11 (16), https://doi.org/10.3390/rs11161840

Chen, X., Huang, Y., Nie, C., Zhang, S., Wang, G., Chen, S., Chen, Z., 2022. A long-term reconstructed TROPOMI solar-induced fluorescence dataset using machine learning algorithms. Sci. Data 9 (1), 427. https://doi.org/10.1038/s41597-022-01520-1

Daumard, F., Goulas, Y., Ounis, A., Pedrós, R., Moya, I., 2015. Measurement and correction of atmospheric effects at different altitudes for remote sensing of sun-induced fluorescence in oxygen absorption bands. IEEE Trans. Geosci. Remote Sens. 53 (9), 5180–5196. https://doi.org/10.1109/TGRS.2015.2418992

Damm, A., Guanter, L., Laurent, V.C.E., Schaepman, M.E., Schickling, A., Rascher, U., 2014. FLD-based retrieval of sun-induced chlorophyll fluorescence from medium spectral resolution airborne spectroscopy data. Remote Sens. Environ. 147, 256–266. https://doi.org/10.1016/j.rse.2014.03.009

Drusch, M., Moreno, J., Bello, U.D., Franco, R., Goulas, Y., Huth, A., Kraft, S., Middleton, E.M., Miglietta, F., Mohammed, G., Nedbal, L., Rascher, U., Schüttemeyer, D., Verhoef, W., 2017. The fluorescence Explorer mission concept—ESA's earth Explorer 8. IEEE Trans. Geosci. Remote Sens. 55 (3), 1273–1284. https://doi.org/10.1109/TGRS.2016.2621820

Emde, C., Buras-Schnell, R., Kylling, A., Mayer, B., Gasteiger, J., Hamann, U., Kylling, J., Richter, B., Pause, C., Dowling, T., Bugliaro, L., 2016. The Libradtran software package for radiative transfer calculations (version 2.0.1). Geosci. Model Dev. 9 (5), 1647–1672. https://doi.org/10.5194/gmd-9-1647-2016

European Space Agency, Sep. 2017a. Technical Assistance for the Deployment of an Advanced Hyperspectral Imaging Sensor During FLEX-EU. https://doi.org/10.5270/ESA-20835d4

European Space Agency, Oct. 2017b. Technical Assistance for the Deployment of an Advanced Hyperspectral Imaging Sensor During SoyFLEX. https://doi.org/10.5270/ESA-50a3dd4

European Space Agency, Apr. 2018. Technical Assistance for the Deployment of an Advanced Hyperspectral Imaging Sensor During SoyFLEX2. https://doi.org/10.5270/ESA-24b3118

European Space Agency, Nov. 2019. Photoproxy: Technical Assistance for the Photosynthetic-Proxy Experiment. https://doi.org/10.57780/esa-bb0ea39

Feret, J.-B., Francois, C., Asner, G.P., Gitelson, A.A., Martin, R.E., Bidel, L.P., Ustin, S.L., Maire, G.L., Jacquemoud, S., 2008. PROSPECT-4 and 5: advances in the leaf optical properties model separating photosynthetic pigments. Remote Sens. Environ. 112 (6), 3030–3043. https://doi.org/10.1016/j.rse.2008.02.012

AERONET FZJ-JOYCE, 2024. AERONET site information database. //aeronet.gsfc.nasa.gov/new_web/photo_db_v3/FZJ-JOYCE.html.

Gastellu-Etchegorry, J.-P., Yin, T., Lauret, N., Cajgfinger, T., Gregoire, T., Grau, E., Feret, J.-B., Lopes, M., Guilleux, J., Dedieu, G., Malenovský, Z., Cook, B., Morton, D., Rubio, J., Durrieu, S., Cazanave, G., Martin, E., Ristorcelli, T., 2015. Discrete anisotropic radiative transfer (DART 5) for modeling airborne and satellite spectroradiometer and LIDAR acquisitions of natural and urban landscapes. Remote Sens. 7 (2), 1667–1701. https://doi.org/10.3390/rs70201667

Guanter, L., Alonso, L., Gómez-Chova, L., Meroni, M., Preusker, R., Fischer, J., Moreno, J., 2010. Developments for vegetation fluorescence retrieval from spaceborne high-resolution spectrometry in the O_2-a and O_2-b absorption bands. J. Geophys. Res. Atmos. 115 (D19), https://doi.org/10.1029/2009JD013716

Gentine, P., Alemohammad, S.H., 2018. Reconstructed solar-induced fluorescence: a machine learning vegetation product based on MODIS surface reflectance to reproduce GOME-2 solar-induced fluorescence. Geophys. Res. Lett. 45 (7), 3136–3146. https://doi.org/10.1002/2017GL076294

Jacquemoud, S., Baret, F., 1990. PROSPECT: a model of leaf optical properties spectra, remote sensing of environment. Remote Sens. Environ. 34 (2), 75–91. https://doi.org/10.1016/0034-4257(90)90100-Z

Jacquemoud, S., Verhoef, W., Baret, F., Bacour, C., Zarco-Tejada, P.J., Asner, G.P., Francois, C., Ustin, S.L., 2009. PROSPECT + SAIL models: a review of use for vegetation characterization. Remote Sens. Environ. 113, S56–S66. https://doi.org/10.1016/j.rse.2008.01.026

Kotchenova, S.Y., Vermote, E.F., Matarrese Jr., R., Frank, J.K., 2006. Validation of a vector version of the 6s radiative transfer code for atmospheric correction of satellite data. Appl. Opt. 45 (26), 6762–6774. https://doi.org/10.1364/AO.45.006762

Kotchenova, S.Y., Vermote, E.F., 2007. Validation of a vector version of the 6s radiative transfer code for atmospheric correction of satellite data. Part II. Homogeneous lambertian and anisotropic surfaces. Appl. Opt. 46 (20), 4455–4464. https://doi.org/10.1364/AO.46.004455

MODIS Atmosphere Science Team, 2017a. MODIS/Terra Aerosol 5-Min L2 Swath 10 km. https://doi.org/10.5067/MODIS/MOD04_L2.061

MODIS Atmosphere Science Team, 2017b. MYD04_L2 MODIS/Aqua Aerosol 5-Min L2 Swath 10 km. https://doi.org/10.5067/MODIS/MYD04_L2.061

Pato, M., Alonso, K., Buffat, J., Auer, S., Carmona, E., Maier, S., Müller, R., Rademske, P., Rascher, U., Scharr, H., 2025. Simulation framework for solar-induced fluorescence retrieval and application to DESIS and hyplant. Remote Sens. Environ. 330, 114944. https://doi.org/10.1016/j.rse.2025.114944

Pato, M., Buffat, J., Alonso, K., Auer, S., Carmona, E., Maier, S., Müller, R., Rademske, P., Rascher, U., Scharr, H., 2024. Physics-based machine learning emulator of at-sensor radiances for solar-induced fluorescence retrieval in the O_2-a absorption band. In: IEEE Journal of Selected Topics in Applied Earth Observations and Remote Sensing, pp. 1–10, https://doi.org/10.1109/JSTARS.2024.3457231

Pato, M., Alonso, K., Auer, S., Buffat, J., Carmona, E., Maier, S., Müller, R., Rademske, P., Rascher, U., Scharr, H., 2023. Fast machine learning simulator of at-sensor radiances for solar-induced fluorescence retrieval with DESIS and hyplant. In: IGARSS 2023–2023 IEEE International Geoscience and Remote Sensing Symposium, pp. 7563–7566, https://doi.org/10.1109/IGARSS52108.2023.10281579

Pinto, F., Celesti, M., Acebron, K., Alberti, G., Cogliati, S., Colombo, R., Juszczak, R., Matsubara, S., Miglietta, F., Palombo, A., Panigada, C., Pignatti, S., Rossini, M., Sakowska, K., Schickling, A., Schüttemeyer, D., Stróżecki, M., Tudoroiu, M., Rascher, U., 2020. Dynamics of sun-induced chlorophyll fluorescence and reflectance to detect stress-induced variations in canopy photosynthesis, plant. Cell Environ. 43 (7), 1637–1654. https://doi.org/10.1111/pce.13754

Rascher, U., Baum, S., Siegmann, B., Buffat, J., Burkart, A., Cogliati, S., Colombo, R., Damm, A., Genesio, L., Hanus, J., Herrera, D., Julitta, T., Knopf, O., Miglietta, F., Muller, O., Quirós Vargas, J., Mar. 2022. FLEXSense: Technical Assistance for Airborne Measurements During the FLEX Sentinel Tandem Experiment, https://doi.org/10.57780/esa-84e5bf5

Sabater, N., Vicent, J., Alonso, L., Verrelst, J., Middleton, E.M., Porcar-Castell, A., Moreno, J., 2018 1551. Compensation of oxygen transmittance effects for proximal sensing retrieval of canopy–leaving sun–induced chlorophyll fluorescence. Remote Sens. 10 (10), https://doi.org/10.3390/rs10101551

Servera, J.V., Rivera-Caicedo, J.P., Verrelst, J., Munoz-Mari, J., Sabater, N., Berthelot, B., Camps-Valls, G., Moreno, J., 2022. Systematic assessment of MODTRAN emulators for atmospheric correction. IEEE Trans. Geosci. Remote Sens. 60, 1–17. https://doi.org/10.1109/TGRS.2021.3071376

Siegmann, B., Alonso, L., Celesti, M., Cogliati, S., Colombo, R., Damm, A., Douglas, S., Guanter, L., Hanus, J., Kataja, K., Kraska, T., Matveeva, M., Moreno, J., Muller, O., Pikl, M., Pinto, F., Quirós Vargas, J., Rademske, P., Rodriguez-Morene, F., Sabater, N., Schickling, A., Schüttemeyer, D., Zemek, F., Rascher, U., 2019. The high-performance airborne imaging Spectrometer hyplant—from raw images to top-of-canopy reflectance and fluorescence products: introduction of an automatized processing chain. Remote Sens. 11 (23), 2760. https://doi.org/10.3390/rs11232760

Rascher, U., Siegmann, B., Krieger, V., Matveeva, M., Quiros, J., Muller, O., Rademske, P., Herrera, D., Baum, S., Miglietta, F., Genesio, L., Colombo, R., Celesti, M., Tudoroiu, M., Cogliati, S., Carotenuto, F., Gioli, B., Genangelli, A., Hanus, J., Houlous, K., Migliavacca, M., Martini, D., Martin, M.P., Carrara, A., Moreno, G., Gonzales-Gascon, R., El-Madany, T., Pacheco-Labrador, J., Damm, A., Ahmed, R., Gupana, R., Paul-Limoges, E., Reiter, I., Xueref-Remy, I., Mevy, J.-P., Santonja, M., Bendig, J., Malenkovsky, Z., Julitta, T., Burkart, A., Jul. 2021. FLEX Sentinel Tandem Campaign: Technical Assistance for Airborne Measurements During the FLEX Sentinel Tandem Experiment, https://doi.org/10.57780/esa-ae7953d

Rascher, U., Siegmann, B., Baum, S., Mar. 2022. HyPlant FLEX Simulator on SAFIRE ATR42 for LIAISE Experiment.

Supercomputing Centre, J., 2021. JURECA: data centric and booster modules implementing the modular supercomputing architecture at jülich supercomputing Centre. J. Large-Scale Res. Facil. 7 (A182), https://doi.org/10.17815/jlsrf-7-182

Tol, C.V.D., Verhoef, W., Timmermans, J., Verhoef, A., Su, Z., 2009a. An integrated model of soil-canopy spectral radiances, photosynthesis, fluorescence, temperature and energy balance. Biogeosciences 6 (12), 3109–3129. https://doi.org/10.5194/bg-6-3109-2009

Tol, C.V.D., Verhoef, W., Rosema, A., 2009b. A model for chlorophyll fluorescence and photosynthesis at leaf scale. Agric. For. Meteorol. 149 (1), 96–105. https://doi.org/10.1016/j.agrformet.2008.07.007

Thompson, D.R., Kahn, B.H., Brodrick, P.G., Lebsock, M.D., Richardson, M., Green, R.O., 2021. Spectroscopic imaging of sub-kilometer spatial structure in lower-tropospheric water vapor. Atmos. Meas. Tech. 14 (4), 2827–2840. https://doi.org/10.5194/amt-14-2827-2021

Thompson, D.R., Bohn, N., Brodrick, P.G., Carmon, N., Eastwood, M.L., Eckert, R., Fichot, C.G., Harringmeyer, J.P., Nguyen, H.M., Simard, M., Thorpe, A.K., 2022. Atmospheric lengthscales for global VSWIR imaging spectroscopy. J. Geophys. Res: Biogeosci. 127 (6), e2021JG006711. https://doi.org/10.1029/2021JG006711

Verhoef, W., Bach, H., 2003. Simulation of hyperspectral and directional radiance images using coupled biophysical and atmospheric radiative transfer models. Remote Sens. Environ. 87 (1), 23–41. https://doi.org/10.1016/S0034-4257(03)00143-3

Vaswani, A., Shazeer, N., Parmar, N., Uszkoreit, J., Jones, L., Gomez, A.N., Kaiser, L., Polosukhin, I., Aug. 2023. Attention Is All You Need. arXiv preprint arXiv:1706.03762.

Verrelst, J., Rivera, J.P., van der Tol, C., Magnani, F., Mohammed, G., Moreno, J., 2015. Global sensitivity analysis of the SCOPE model: what drives simulated canopy-leaving sun-induced fluorescence? Remote Sens. Environ. 166, 8–21. https://doi.org/10.1016/j.rse.2015.06.002

Verrelst, J., Sabater, N., Rivera, J.P., Muñoz-Marí, J., Vicent, J., Camps-Valls, G., Moreno, J., 2016. Emulation of leaf, canopy and atmosphere radiative transfer models for

fast global sensitivity analysis. Remote Sens. 8 (8), 673. https://doi.org/10.3390/rs8080673

Verrelst, J., Caicedo, J.P.R., Muñoz-Marí, J., Camps-Valls, G., Moreno, J., 2017. SCOPE-based emulators for fast generation of synthetic canopy reflectance and sun-induced fluorescence spectra. Remote Sens. 9 (9), 927. https://doi.org/10.3390/rs9090927

Wieneke, S., Ahrends, H., Damm, A., Pinto, F., Stadler, A., Rossini, M., Rascher, U., 2016. Airborne based spectroscopy of RED and far-RED sun-induced chlorophyll fluorescence: implications for improved estimates of gross primary productivity. Remote Sens. Environ. 184, 654–667. https://doi.org/10.1016/j.rse.2016.07.025

Yang, P., Van Der Tol, C., 2018. Linking canopy scattering of far-red sun-induced chlorophyll fluorescence with reflectance. Remote Sens. Environ. 209, 456–467. https://doi.org/10.1016/j.rse.2018.02.029

Yang, P., van der Tol, C., Verhoef, W., Damm, A., Schickling, A., Kraska, T., Muller, O., Rascher, U., 2019. Using Reflectance to Explain Vegetation Biochemical and Structural Effects on Sun-Induced Chlorophyll Fluorescence, Remote Sensing of Environment, https://doi.org/10.1016/j.rse.2018.11.039